Tectonics

RESEARCH ARTICLE
10.1029/2019TC005997

Key Points:
- In the Andean volcanic arc, margin-parallel and blind oblique fault systems control volcanic, hydrothermal, and ore-porphyry processes
- Subsurface conductivity structure and seismicity show a WNW trending active fault in the Andean Southern Volcanic Zone
- Results show magmatic/hydrothermal fluids are compartmentalized by local faults and elevated fluid pressures promote fault reactivation

Supporting Information:
- Supporting Information S1
- Data Set S1

Correspondence to:
R. K. Pearce,
r.pearce.11@ucl.ac.uk

Citation:
Pearce, R. K., Sánchez de la Muela, A., Moorkamp, M., Hammond, J. O. S., Mitchell, T. M., Cembrano, J., et al. (2020). Reactivation of fault systems by compartmentalized hydrothermal fluids in the Southern Andes revealed by magnetotelluric and seismic data. *Tectonics*, *39*, e2019TC005997. https://doi.org/10.1029/2019TC005997

Received 21 NOV 2019
Accepted 12 OCT 2020
Accepted article online 29 OCT 2020

Reactivation of Fault Systems by Compartmentalized Hydrothermal Fluids in the Southern Andes Revealed by Magnetotelluric and Seismic Data

R. K. Pearce[1], A. Sánchez de la Muela[2,1], M. Moorkamp[3], J. O. S. Hammond[2], T. M. Mitchell[1], J. Cembrano[4], J. Araya Vargas[4,5], P. G. Meredith[1], P. Iturrieta[6], N. Pérez-Estay[5], N. R. Marshall[7], J. Smith[8], G. Yañez[4], W. Ashley Griffith[9], C. Marquardt[4], A. Stanton-Yonge[1,4], and R. Núñez[4]

[1]Earth Science, University College London, London, UK, [2]Department of Earth and Planetary Sciences, Birkbeck, University of London, London, UK, [3]Department of Earth and Environmental Sciences, Ludwig Maximilians University of Munich, Munich, Germany, [4]Departamento de Ingeniería Estructural y Geotécnica, Pontificia Universidad Católica de Chile, Santiago, Chile, [5]Centro de Excelencia en Geotermia de los Andes (CEGA), Universidad de Chile, Santiago, Chile, [6]Helmholtz Centre Potsdam, GFZ German Research Centre for Geosciences, Potsdam, Germany, [7]Department of Earth Sciences, University of Oxford, Oxford, UK, [8]Division of Geological and Planetary Sciences, California Institute of Technology, Pasadena, CA, USA, [9]School of Earth Sciences, Ohio State University, Columbus, OH, USA

Abstract In active volcanic arcs such as the Andean volcanic mountain belt, magmatically sourced fluids are channeled through the brittle crust by faults and fracture networks. In the Andes, volcanoes, geothermal springs, and major mineral deposits have a spatial and genetic relationship with NNE trending, margin-parallel faults and margin-oblique, NW trending Andean Transverse Faults (ATF). The Tinguiririca and Planchón-Peteroa volcanoes in the Andean Southern Volcanic Zone (SVZ) demonstrate this relationship, as their spatially associated thermal springs show strike alignment to the NNE oriented El Fierro Thrust Fault System. We constrain the fault system architecture and its interaction with volcanically sourced hydrothermal fluids using a combined magnetotelluric (MT) and seismic survey that was deployed for 20 months. High-conductivity zones are located along the axis of the active volcanic chain, delineating fluids and/or melt. A distinct WNW trending cluster of seismicity correlates with resistivity contrasts, considered to be a reactivated ATF. Seismicity occurs below 4 km, suggesting activity is limited to basement rocks, and the cessation of seismicity at 9 km delineates the local brittle-ductile transition. As seismicity is not seen west of the El Fierro fault, we hypothesize that this structure plays a key role in compartmentalizing magmatically derived hydrothermal fluids to the east, where the fault zone acts as a barrier to cross-fault fluid migration and channels fault-parallel fluid flow to the surface from depth. Increases in fluid pressure above hydrostatic may facilitate reactivation. This site-specific case study provides the first three-dimensional seismic and MT observations of the mechanics behind the reactivation of an ATF.

1. Introduction

The ascent of magmatically sourced fluids through the brittle crust is facilitated by inherited planes of weakness, such as lithospheric scale fault systems (Cembrano & Lara, 2009; Nakamura, 1977; Shaw, 1980). Within these fault systems, highly permeable networks of interconnected fault damage zones act as fluid conduits (Faulkner et al., 2010). Conversely, variations in pressure, temperature, and composition of fluids in the fracture network can lead to fracture sealing and cementation, as mineral precipitation during fluid transport decreases the permeability of the fault core (e.g., Cox, 2005; Micklethwaite et al., 2010). This causes the maximum flow direction to orient parallel to the fault plane (Caine et al., 1996; Faulkner et al., 2010). Simultaneously, the migration and accumulation of fluids within these fault systems play a key role in the nucleation of earthquakes, as increased pore fluid pressures reduce the effective normal stress projected on a fault plane, consequently increasing its probability of failure (Cox, 2010, 2016; Roquer et al., 2017; Sibson, 1985). These interdependent processes result in episodic and anisotropic migration of fluids within fault zones, along with the heterogeneous distribution of hydromechanical properties therein (Cox, 2010; Rowland & Sibson, 2004; Sibson, 1996, 2004).

In an active volcanic arc, this complex interaction between hydrothermal fluids and structural systems can significantly influence tectonomagmatic processes, such as the distribution of volcanoes (Cembrano & Lara, 2009; Nakamura, 1977; Sielfeld et al., 2017; Tibaldi, 2005), the emplacement of ore deposits and plutons (Hedenquist & Lowenstern, 1994; Piquer et al., 2016), the localized structural and geochemical development of geothermal springs and fumaroles (Sanchez et al., 2013; Sibson, 1996; Tardani et al., 2016; Veloso et al., 2019), and the location, magnitude, frequency, and timing of crustal seismicity (Cox, 2016). Geophysical studies can image these active structural and hydromagmatic systems in order to map their architecture as a function of depth. In particular, magnetotelluric (MT) surveys map electrical conductivity domains that are commonly related to the presence or absence of fluids with different degrees of salinity or partial melt at a crustal scale (Pommier, 2014; Simpson & Bahr, 2005). When combined with local seismic hypocenter locations, the spatial coherency of anomalous conductors and seismogenic features can reveal interacting hydrothermal fluids and seismically active fault systems in a volcanic regime (e.g., Becken & Ritter, 2012; Bertrand et al., 2012; Wannamaker et al., 2009).

The overall aim of this study is to image and constrain the architecture of a major fault system within a volcanic arc using a combined MT and seismicity survey. This site-specific case study will be used to analyze the relationship between actively deformating faults and their role in fluid transport and storage throughout the upper crust. This objective was achieved by conducting spatially and temporally overlapping MT and seismic surveys in a field study area within the Andean Southern Volcanic Zone (SVZ), which encompasses the Tinguiririca and Planchón-Peteroa Volcanic complexes (PPVCs; 70.4–70.9°W and 34.65–35.2°S). In this region, significant evidence of interdependent tectonic-hydrothermal processes has been reported. For example, a prominent geothermal reservoir found at the western flank of the Tinguiririca volcanic complex has been considered for geothermal energy exploitation (Aravena et al., 2016; Benavente et al., 2016; Clavero et al., 2011; Pritchard et al., 2013). Furthermore, the PPVC, which has been episodically on yellow alert due to degassing and ash expulsion events since 2011 (Aguilera et al., 2016; GVP, 2020), demonstrates a NNE strike alignment of eruptive vents and proximal geothermal springs along the major El Fierro Fault System (EFFS) that outcrops within the field area (Giambiagi et al., 2019; Mescua et al., 2013; Pavez et al., 2016; Piquer et al., 2019). The region of the SVZ is of particular interest due to the presence of both convergent margin-parallel fold-thrust belt systems such as the EFFS, and margin-oblique WNW and ENE trending features, referred to as Andean Transverse Faults (ATF) (Cembrano & Lara, 2009; Katz, 1971). Although significant geological and geochemical evidence indicates that these margin-oblique structures exert control on volcanism (Cembrano & Lara, 2009; Lara et al., 2004; Piquer et al., 2019; Sielfeld et al., 2017), hydrothermal system dynamics (Lara et al., 2004; Sanchez-Alfaro et al., 2015), and ore-porphyry deposition (Chernicoff et al., 2002; Sillitoe, 1997), the subsurface interactions of these processes are poorly understood.

2. Margin Parallel and Oblique Fault Systems in the Southern Andes

The Andes comprise of a volcanically active mountain belt along the western margin of South America between latitudes 18–46°S, which have formed from the roughly eastward convergence and subduction of the oceanic Nazca Plate beneath the South American Plate since the Jurassic (ca. 180 Ma) (Charrier et al., 2007; Mpodozis & Cornejo, 2012; Pardo et al., 2009; Ramos, 2010). Since the Miocene (<20 Ma), orogenic uplift was coupled with intense volcanism and the formation of an eastward migrating volcanic arc. The relative plate convergence velocity of 6.6 cm/year has had a trend of N78°E since the Holocene (<12 Ma) (Angermann et al., 1999). The Andean western margin is characterized by (a) over 200 Pleistocene-Holocene stratovolcanoes throughout its volcanic arc (60 of which have been active during the Holocene) (Stern, 2007); (b) megathrust earthquakes that reach magnitudes >Mw 8, such as the Mw 9.5 Valdivia and Mw 8.8 Maule earthquakes in 1960 and 2010, respectively (Bonali et al., 2013); (c) giant Cu-Au-Ag porphyry ore deposits (Chernicoff et al., 2002; Sillitoe, 1997); and (d) up to 16,000 MWe of potential high-enthalpy geothermal resources (Aravena et al., 2016; Sanchez-Alfaro et al., 2015). Figure 1 shows the major NNE trending margin-parallel volcanic arc, and the distribution of ore deposits, geothermal springs, and oblique lineaments along the Southern Andes. Throughout this region, volcanoes, geothermal springs, and the locations of major mineral deposits are spatially coherent with the first-order NNE oriented structural systems in the High Andes (Ramos, 2010). An exception is the region between 28°S and 33°S referred to as the Pampean Flat Slab Segment, where shallow subduction angles

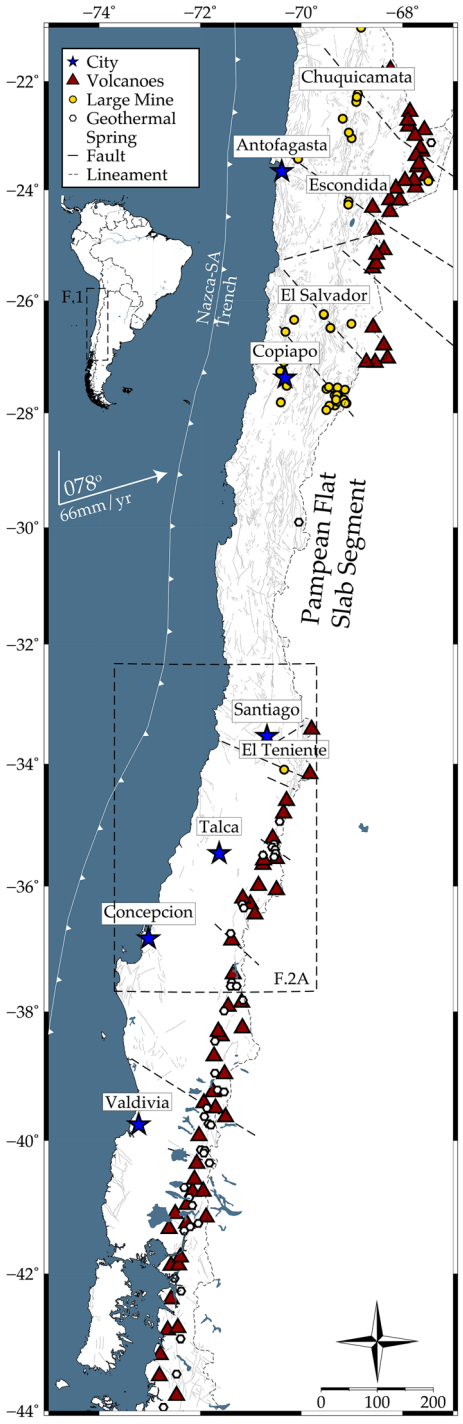

Figure 1. Map of the Andean volcanic chain between latitudes 21.5° and 44°S. See legend in top-left corner for description of symbols. Localities of active volcanoes are sourced from the Smithsonian Institute Holocene Volcanic database, geothermal areas from (2016), faults and major mines from Sernageomin (2003), northern lineaments (21.5–28°S) sourced from Richards et al. (2001), southern lineaments from Cembrano and Lara (2009), and plate vector from Angermann et al. (1999). The frame overlying the map between latitudes 32–38°S indicates the location of Figure 2a.

prevented the formation of a mantle wedge, resulting in a break in the volcanic arc (Mpodozis et al., 1989). The porphyry-copper provinces are younger in age toward the south; the metallogenic belts in the north, including the Chuquicamata and Escondida mines, formed during the late Eocene-early Oligocene (38–35 Ma) (Richards et al., 2001), whereas the southernmost mapped mine, El Teniente, is from an ore province that formed during late Miocene-early Pliocene (10–4 Ma) (Piquer et al., 2015).

Second-order NW trending transverse structural domains that crosscut the volcanic arc have been observed throughout the Andes and are considered to be pre-Andean, inherited basement faults (e.g., Katz, 1971; Lara et al., 2006; Melnick & Echtler, 2006; Piquer et al., 2017; Yáñez et al., 1998). These seismically active ATF (Aron et al., 2015; Sielfeld et al., 2019; Stanton-Yonge et al., 2016) accommodate part of the deformation arising from oblique convergence (Perez-Flores et al., 2016; Stanton-Yonge et al., 2016), are spatially and genetically associated with massive to medium scale ore deposits (e.g., Chernicoff et al., 2002; Mpodozis & Cornejo, 2012; Piquer et al., 2015), and are believed to control the seismic segmentation of the plate interface (Melnick et al., 2009).

Within the volcanic arc, ATF are considered to influence magmatic processes, as volcanic and intrusive body emplacement show alignment with the strike of ATF domains (Acocella et al., 2011; Cembrano & Lara, 2009; Viramonte et al., 1984). These ATF are enigmatic due to their WNW orientation with respect to the current plate convergence vector, which promotes a bulk transpressive stress regime. This makes them unfavorable for dilation that facilitates magma ascent through the crust (Cembrano & Lara, 2009). However, these WNW trending faults are nearly optimally oriented to accommodate sinistral-reverse displacement (Stanton-Yonge et al., 2016). Recent investigations have determined that these structures store overpressurized fluids derived from deep magmatic roots, thus impact the architecture and distribution of active volcanic and hydrothermal systems across the Andes (Sanchez et al., 2013; Sielfeld et al., 2019; Tardani et al., 2016; Veloso et al., 2019; Wrage et al., 2017). Furthermore, the interaction between NNE trending fault systems and ATF at the SVZ controls the conditions required to develop and sustain a shallow hydrothermal system, where fluids within conduits associated with ATF are stored and overpressurized (Perez-Flores et al., 2017; Roquer et al., 2017).

The intersection of major NNE oriented fault systems and the potentially blind, discrete WNW trending ATF domains occur across all latitudes of the Andes, showing an along-strike spatial control of major mineral deposits (Katz, 1971; Sillitoe, 1997). Sillitoe (1997) and Piquer et al. (2019) suggested that hydrothermal minerals related to porphyry copper deposits of central Chile are formed at such intersections. As the surface expressions of the ATF are limited to a few scarce outcrops (Lara et al., 2004; Perez-Flores et al., 2016), they are mostly inferred from kilometer-scale topographic lineaments (Cembrano & Lara, 2009; Giambiagi et al., 2019; Moreno, 1976; Piquer et al., 2016), major magnetic anomalies (Yáñez et al., 1998), and alignment of seismicity and volcanic morphological features (Aron et al., 2015; Lara et al., 2004; Sielfeld et al., 2017).

The setting of this study is the Andean SVZ, which features margin parallel fault systems, margin-oblique ATF system, and fault-strike aligned

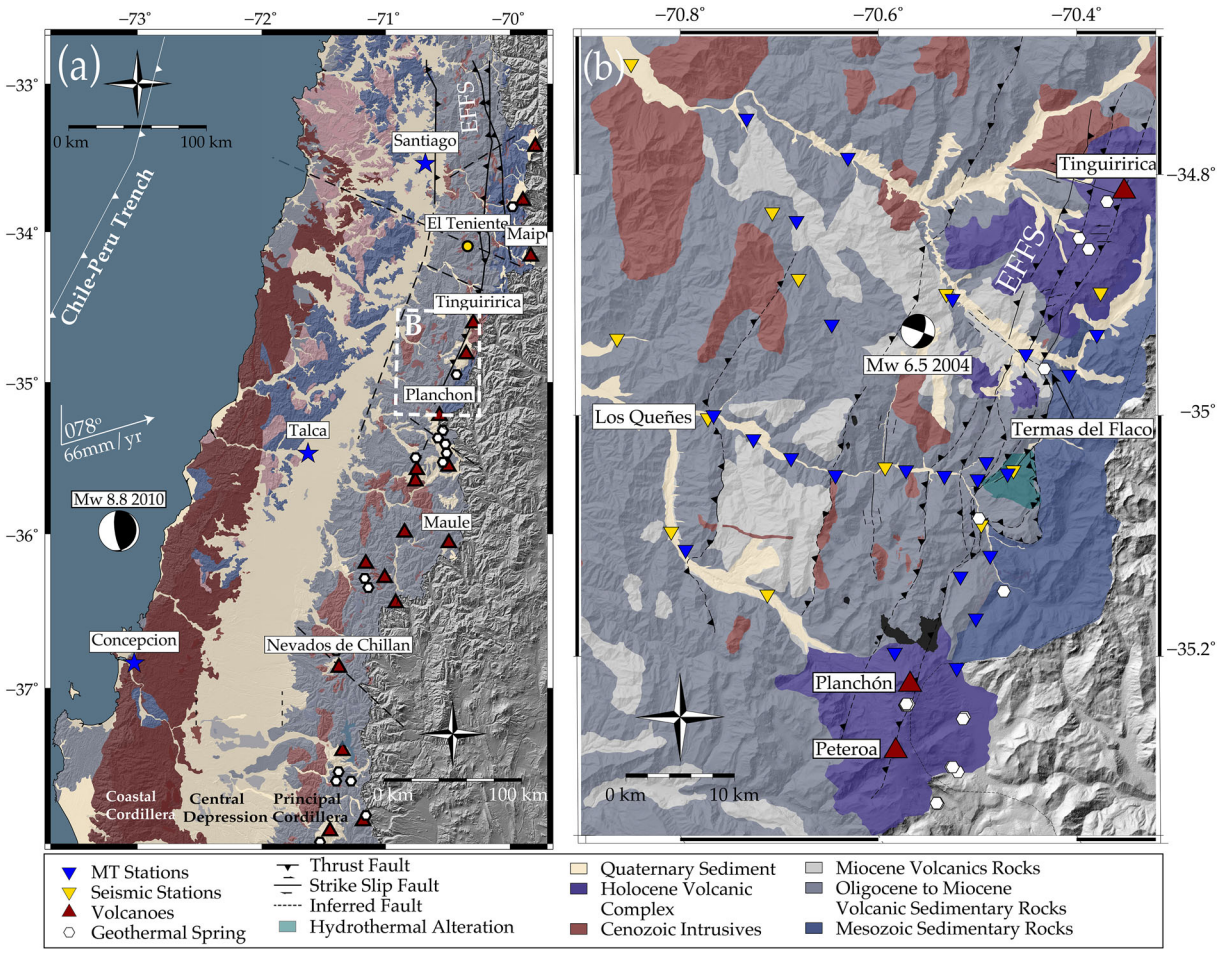

Figure 2. (a) Regional scale geology of the Andes of central-southern Chile and of the Southern Volcanic Zone. See legend for a description of all symbols. The geological units and the El Teniente mine location are from Sernageomin (2003), and focal mechanisms of the Maule and Teno earthquakes are after Ekstrom et al. (2012). Frame labeled B in (a) indicates the location of Figure 2b. (b) Local geological map of the field study area from Núñez Tapia (2018) and distribution of magnetotelluric and seismic stations within the geophysical survey grid. Digital Elevation Model (DEM) from PALSAR (2011).

volcanic complexes. The geological, geophysical, and geochemical signatures of these domains indicate that these faults and volcanic systems have interdependently evolved during the orogenesis of the Andes; however, their interaction at depth remains unresolved. This study provides a high-resolution 3-D model of an area characterized by these structural and volcanic systems, with the aim to improve our understanding of their nature within upper crustal depths.

3. Regional Context and Geology

The Andes are segmented from north to south into Northern, Central, Southern, and Austral Volcanic Zones, due to the latitudinal variation of altitude, crustal thickness, convergence rate, plate coupling, volcanism, and climate (Ramos, 2010). The selected field area for this study is in the SVZ in the Principal Cordillera (Figure 2a). In this region, the main morphotectonic features of the Chilean Andes are the western Coastal and eastern Principal Cordillera, which are divided by the Central Depression (Figure 2a) (Charrier et al., 2015; Ramos et al., 2014). The EFFS is the major structural feature in the region, which thrusts the Miocene volcanic sequences eastward over an exposed sequence of Mesozoic sedimentary units (Farias et al., 2010). The surveyed study area is located at the western limit of the Chilean Principal Cordillera at this Meso-Cenozoic boundary (Figure 2b). This boundary is characterized by a heat flow regime of 200 mW/m^2, which is anomalously high compared to the heat flow regime of 60 mW/m^2 in the surrounding western and northwestern Andes (Benavente et al., 2016). This high heat flow gradient occurs as the eastward migrating

volcanic arc is partially situated beneath the Principal Cordillera. Thus, volcano-magmatic processes, such as the development of major stratovolcanoes and geothermal fluid outflow springs, are concentrated in the High Andes (Figure 1) (Benavente et al., 2016). The Tinguiririca geothermal outflow spring and the PPVC are within the limits of the geophysical survey grid (Figure 2b).

3.1. Hydrothermal and Magmatic Systems of the Tinguiririca and Planchón-Peteroa Stratovolcanic Complexes

The Tinguiririca volcanic complex (TVC) (Figure 2b) is a Holocene cluster of 10 scoria cones that overlay a lower to middle Pleistocene plateau of andesitic lavas, directly above the NNE trending EFFS (Stern, 2007). Tinguiririca's potential for geothermal exploitation has been evaluated with MT (Lira Martínez, 2011), seismic (Clavero et al., 2011), geochemical (Benavente et al., 2016), and borehole methods (Droguett et al., 2012). These studies reveal a deep geothermal reservoir with a volume of 5–25 km^3 contained by a low-resistivity hydrothermally altered argillic clay cap at 3–6 km depth (Aravena et al., 2016; Lira Martínez, 2011). Current thermal activity in proximity of Tinguiririca include high elevation fumaroles and lowland chloric springs, such as the major outflow spring Termas del Flaco, a sulfur-rich mud pool that is commercially exploited (Figure 2b) (Benavente et al., 2016; Pavez et al., 2016). The geochemical signatures of these springs and high-altitude fumaroles indicate that the reservoir's temperatures range from 230–250°C, bearing trace elements of shallow meteoric aquifers and deep source magmatic gasses (Aravena et al., 2016; Benavente et al., 2016; Pavez et al., 2016). Fumarolic discharge also shows typical signatures of a hydrothermal system, including water vapor, concentrations of CH_4, H_2, and H_2S, and magmatic arc type gases (Benavente et al., 2016). Based on these observations, it is interpreted that a 2–6 km-deep reservoir related to the Tinguiririca volcano is recharged by the circulation of shallow meteoric and deep magmatic fluids (Benavente et al., 2016; Giambiagi et al., 2019; Pavez et al., 2016).

The PPVC (Figure 2b) consists of a series of Pleistocene-Holocene stratovolcanoes with two main volcanic centers: Planchón (14 ka) and Peteroa (<7 ka) (Tassi et al., 2016). Like the Tinguiririca volcano, these volcanic edifices are emplaced along the trace of the EFFS. The composition of the PPVC progresses from earliest stage basaltic lavas to bimodal basaltic-andesitic and dacitic magmas extruded as subplinian explosions (Stern, 2007). Fumarolic discharge and acid crater lakes are proximal to the edifice, with chemical signatures of a hydrothermal system recharged by meteoric waters, which also bear He signatures indicative of deeper magma-derived fluid sources (Benavente et al., 2016). A phreatic eruption accompanied by ash discharge occurred from August 2010 to June 2011, placing Planchón-Peteroa on yellow alert eruption warning that is still in place. Subsequent tephra fall contained altered Fe oxides and Cu minerals but no juvenile magmatic constituents, indicating that hydrothermal fluid migration drove the phreatic eruption and tephra production. This eruption stage was followed by sporadic ash and vapor emission, which were hydrothermally sourced, and bore traces of deep oxidized magmatic fluids. These magmatic traces, including SO_2, HCl, and HF, contained signatures of a highly degassed (old) magmatic body (Tassi et al., 2016). It has since experienced sporadic events of degassing, water-vapor expulsion, and shallow seismic tremors, the most notable of which are a Mw 4 earthquake that occurred 4–7 km beneath the summit on 8 July 2017 and an explosive ash emission in September 2018 (GVP, 2020).

3.2. Faulting, Kinematics, and Hydrothermal Alteration

The largest structural feature in the study area is a segment of the NNE trending, 200 km long EFFS, a steeply dipping, reverse fault that formed during the late-Eocene to Oligocene. Reverse faulting deformation initiated when thickening of the lower crust was assisted by magmatic softening, and arc rocks were subsequently displaced eastward and uplifted along this fault (Charrier et al., 2002; Godoy & Lara, 1994; Gow & Walshe, 2005). Structural analysis of this fault system suggests that, while the dominant structure formed from reverse faulting, its current kinematics are dextral strike slip under regional transpression (Giambiagi et al., 2019). Outcropping fault strands of the EFFS show distinct alignment with volcanic and geothermic features in the area (Figure 3a). Additionally, significant hydrothermal alteration is seen in the Oligocene to Miocene volcanic and sedimentary rocks, spatially related to the hanging wall of the EFFS (Figure 3c). The alteration in this zone is of philic-argillic type, with pervasive pyrite veinlets. The alteration appears to be strongly controlled by lithology, where the more fractured and permeable units exhibit stronger alteration. Additionally, it shows evidence of a supergene alteration, which produces oxidation

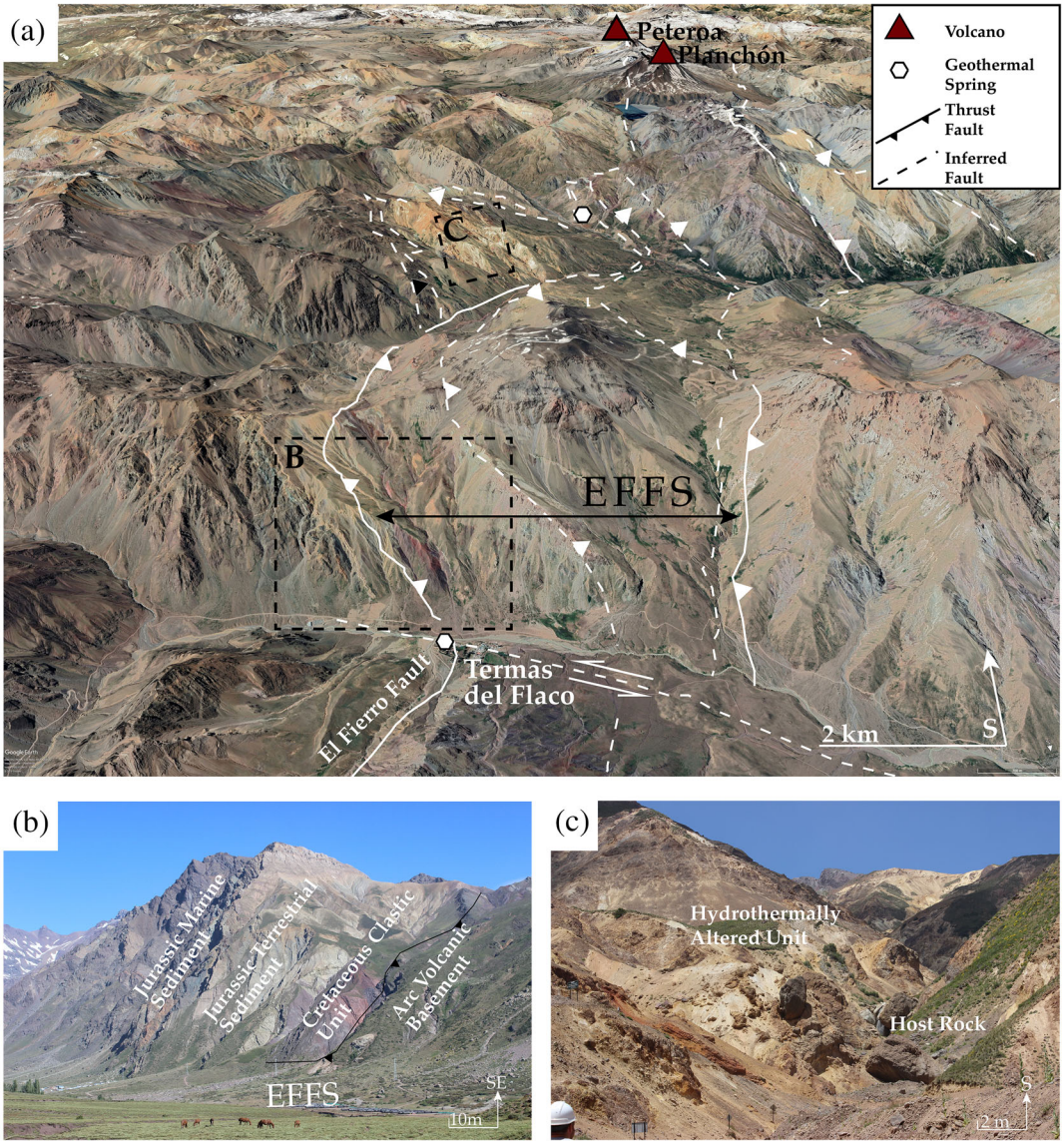

Figure 3. (a) Satellite image of the field area looking SSE, displaying the primary features of interest; the trace of El Fierro thrust fault system is taken from Pavez et al. (2016), and inferred sinistral strike-slip faults (potential ATF) from Giambiagi et al. (2019). The larger and smaller black frames in (a) indicate the locations of (b) and (c), respectively. (b) Photo showing the high angled El Fierro fault plane creating the unconformity between the Jurassic sediments and Quaternary volcaniclastics. (c) Photo showing hydrothermally altered, Oligocene-Miocene volcanic host rock at the EFFS fault zone.

and leaching of sulfides (i.e. pyrite), forming limonites (Jarosite > Goethite> Hematite). This alteration is restricted to the strands and footwall of the El Fierro fault (Figures 3a and 3c).

Previous seismic tomography studies south of Tinguiririca volcano have inferred that the permeable damage zones of the EFFS act as channels for meteoric- and magmatic-derived fluids into the geothermal fields and outflow springs (Pavez et al., 2016). The presence of fluids in a porous and fractured media in the EFFS was inferred due to the presence of high *Vp*/*Vs* ratios. When combined with geochemical analyses of fumarolic discharges (Benavente et al., 2016), these results suggest that an active deep andesitic magmatic system underlies an upper hydrothermal zone located at 2–3 km depth. These studies conclude that a magmatic reservoir is emplaced between 6–9 km depths (3–6 km below sea level in the research article), and that the EFFS is a conduit for fluid mobility. This interpretation has recently been debated by Giambiagi et al. (2019), who combined paleostress analysis, structural mapping, and boundary element modeling methods to

characterize the Tinguiririca geothermal fields, specifically the mechanisms that control fluid migration in this hydromagmatic system. They state that a blind NNE oriented strike-slip fault at 2.5 km depth within the EFFS volume controls the migration of fluids, due to strong directional permeability that occurs at the fault intersection with surrounding strands of the EFFS. This blind fault acts to localize hydrothermal fluid circulation, which in turn increases the fault's probability of failure due to increased pore fluid pressures along the fault plane. This became apparent when a seismic swarm in 2010 highlighted the geometry of this blind fault plane (Lira Martínez, 2011). The 2010 seismic swarm is considered to be related to local stress redistribution from the 2004 6.5 Mw earthquake (Figure 2b). From this event, along with local paleostress analysis in the Tinguiririca valley, an ESE oriented sinistral strike slip regime is assumed to dominate this region (Giambiagi et al., 2019).

4. Geophysical Data Acquisition and Processing

MT is a geophysical method that uses naturally occurring electromagnetic fields to estimate the electrical conductivity structure of the subsurface (Chave & Jones, 2012; Simpson & Bahr, 2005). Coupled with MT, precise hypocenter locations in seismically active areas can be used to infer the location, geometry, and distribution of active faults that may interact with crustal fluids (Held et al., 2016; Ingham et al., 2009; Legrand et al., 2011; Wannamaker et al., 2009). For these reasons, this study combines seismic hypocenters with a 3-D model of conductivity structure.

4.1. MT Survey, Data Processing, and Inversion

In MT, naturally occurring electromagnetic fields incident on the Earth's surface are passively and independently measured as a continuous time series of two horizontal electric components, *Ex*, *Ey*, and two horizontal magnetic components, *Hx* and *Hy*. When converted into the frequency domain, the response of the electric current to a varying magnetic field is quantified as the complex impedance tensor as a function of frequency, $Z\omega$. The impedance responses are then used to model conductivity variations of the Earth's subsurface through the relation $E = ZH$ (Simpson & Bahr, 2005).

The field campaign involved the collection of 26 broadband induction coil MT sites with approximately 5 km spacing in a 40 km^2 field area (Figure 2b). At all MT stations, the north-south (x) and east-west components (y) of the electric and magnetic fields were independently measured, as well as a vertical component of the magnetic field. MT data were collected using Metronix ADU-07e systems equipped with MFS-06e or MFS-07e coils. The experiment sampled at 1024 Hz for an initial 30 min, after which data were collected at a 128 Hz sampling rate for 48 hr. As the features of interest in this study are concentrated in the eastern limits of the surveyed area, namely, the EFFS and the along-strike TVC and PPVC, the MT grid has a dense NS oriented transect in this sector, while three EW oriented transects were deployed to act as regional controls. The data processing method used was the Bounded Influence Remote Referencing (BIRRP) program (Chave, 1989; Chave & Thomson, 2003). This well-established MT data processing algorithm uses statistically robust techniques and remote referencing to yield the impedance responses at selected frequencies. Of the completed 26 sites, data from three stations have been discarded due to irreparably poor data quality attributed to cultural and natural noise contamination, such as electric dipole interference or current channeling, respectively. Some data sets also feature Galvanic Distortion, which is caused by near-surface conductivity heterogeneities at the measurement site (Bibby et al., 2005). The period bands affected by high levels of artificial noise were masked by assigning high error values to the data points in order to reduce the impact of noisy data on the inversion results. An example of this effect is observed in the *YX* component of the 3–20 s period band of Station 2 in Figure 4. The 3D inversion of the 23 station MT grid was performed with a quasi-Newton optimization method that minimizes the data misfit and Tikhonov-type regularization parameter (Avdeev, 2005; Avdeev & Avdeeva, 2009). The algorithm uses joint inversion methods to correct for galvanic distortion inherent in the data. The distortion correction multiplies the frequency-independent, real valued distortion matrix, C, to the complex, frequency-dependent impedance tensor in the form $Z_{obs} = CZ$ (Avdeeva et al., 2015).

The initial model mesh comprised $80 \times 80 \times 30$ cells, with cell dimensions of 1,000 m × 1,000 m × 100 m that was increased by a factor 1.1 times the vertical cell length per layer. The inversion was conducted with an error floor of 5% for the impedance data sets and a large regularization parameter that was reduced by 1 order of magnitude per inversion run. Homogeneous meshes with initial conductivities 100, 500 and

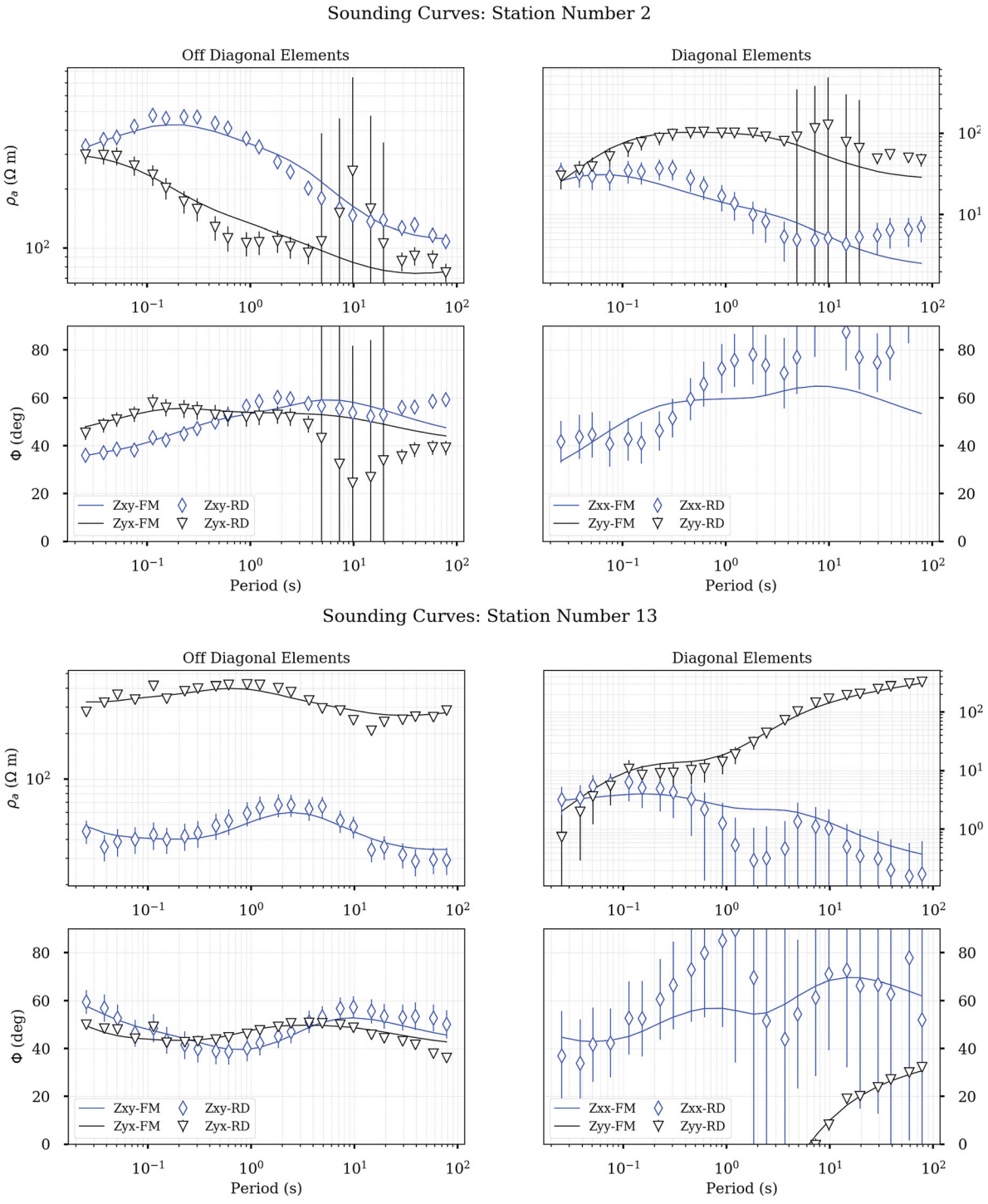

Figure 4. Magnetotelluric apparent resistivity and phase results for all impedance tensor components (Z_{xx}, Z_{xy}, Z_{yx}, and Z_{yy}) as a function of period (s) for Stations 2 and 13. Within each graph, black inverted triangles and blue diamonds show the data, and black and blue lines (FM) are the responses of our preferred model.

1,000 Ωm were used as starting models to conduct full inversions and to produce layered models based on the 1D inversion of the average of the data set. The layered models all resulted in a mesh of an overall 500 Ωm resistivity with a 50–100 Ωm layer between 8 and 14 km. This layered model was the starting mesh for the final model that was selected for further analysis. The final preferred model, which was obtained after 800 iterations, reduced the RMS from a value of 9 to 1.55. The conductivity structures that emerged

in this model was also observed in models with other initial conductivities, which supports the robustness of the result. While the RMS is a good overall measure of the fit between the inversion model and the real data, we also examine the closeness between the sounding curves of both data sets for individual stations (Miensopust et al., 2013).

An example of the real data and model fit for Stations 2 and 13 is provided in Figure 4, which show the apparent resistivities and phases for all impedance components (Z_{xx}, Z_{xy}, Z_{yx}, and Z_{yy}) across 0.01–100 s period bands. The results for Station 2 show that the model and real data sets fit well, apparent as the inversion model data and real data (labeled FM and RD on Figure 4, respectively) closely match across all period bands. The Z_{yx} component of Station 2 (Figure 4) shows some scatter around the 3–12 s period band, but this does not affect the inversion model due to the high errors assigned to these data points. The off-diagonal components of Station 13 exhibit some Galvanic Distortion, apparent as Z_{yx} is shifted to an apparent resistivity above Z_{xy} by approximately one magnitude across all period bands. As discussed, this type of Galvanic distortion is accounted for in the joint inversion by the distortion tensor, and the inversion model data (FM; Figure 4) and real data (RD; Figure 4) fit well despite the distortion, as was the case for all Galvanically distorted datasets (see the supporting information for the real and model data fits for each station). Furthermore, sensitivity tests were carried out to verify the robustness of each conductive structure within the model (see the supporting information on these techniques).

4.2. Seismic Survey and Hypocenter Location

A network of 12 broadband seismometers (six Güralp CMG-6TDs and six Güralp CMG- 3ESPCDs) was deployed from April 2017 until December 2018 (Hammond et al., 2017). Average interstations spacing was approximately 15 km, with site localities complimenting the MT stations distribution (Figure 2b). Hypocenters were automatically detected using the software package QuakeMigrate (QMigrate; https://github.com/QuakeMigrate/QuakeMigrate), which scans the seismic trace at each station by determining a STA/LTA onset function with high values representing phase arrivals (Drew et al., 2013; Smith et al., 2020). The onset functions are then backpropagated in a traveltime grid determining a 4D function representing the combined onsets spatially and temporally. When the maximum coalescence value exceeds a user-defined threshold value, an event is triggered. A marginal window, representing the expected model error, is taken about each event with the 4D coalescence stacked in the time domain to give a probability map of the earthquake location. Events are then filtered using the local- and global-Gaussian error ellipses, with events with a large global- to local-Gaussian ratio rejected as they represent false triggers. This procedure outputs an automated catalog of earthquake locations, expected location uncertainties, and phase arrivals. The resulting QuakeMigrate catalog was visually inspected afterward, to manually update *P* and *S* wave arrivals. These revised traveltime picks were then used to estimate hypocenters using HYPOINVERSE-2000 (Klein, 2002).

Earthquake locations are sensitive to the velocity model used. We initially located a portion of our earthquakes catalog using the velocity model calculated for the Southern Andes Volcanic Zone by Sielfeld et al. (2019). From this we obtained 205 hypocenters, with horizontal error <2 km and vertical error <5 km, azimuthal gap 87–336° and residuals (RMS) of 0.01–0.29 s. The model was then updated by iteratively inverting for the resulting locations and the initial 1-D velocity model using VELEST (Kissling et al., 1994). VELEST allowed to iteratively improve the RMS misfit between calculated and observed traveltimes of each solution through updating the velocity model and relocating the earthquakes. Five different a priori models were tested including constant velocity models and CRUST1.0. All models showed similar trends, requiring a low-velocity shallow crust, but the modified 1D velocity model of Sielfeld et al. (2019) proved to be the best model with the lowest RMS misfit.

The final model used in this study is shown in Figure 5. The homogeneous velocity layers in our best solution model were converted into gradient velocity layers, to reduce the depth-clustering effect that sharp velocity discontinuities have on hypocenter location due to seismic rays being modeled as refracted from discontinuities, instead of realistic downgoing rays with spread emergence angles (Klein, 2002). This resulted in location of 1,369 hypocenters with a mean horizontal error of 0.92 and 1.68 km mean vertical error. To provide more detailed estimates of locations, the traveltime data were reprocessed using the double-difference algorithm in HypoDD (Waldhauser & Ellsworth, 2000). This minimizes the sensitivity of source location to the velocity model and allows identification of trends in the data with more accuracy (although with absolute

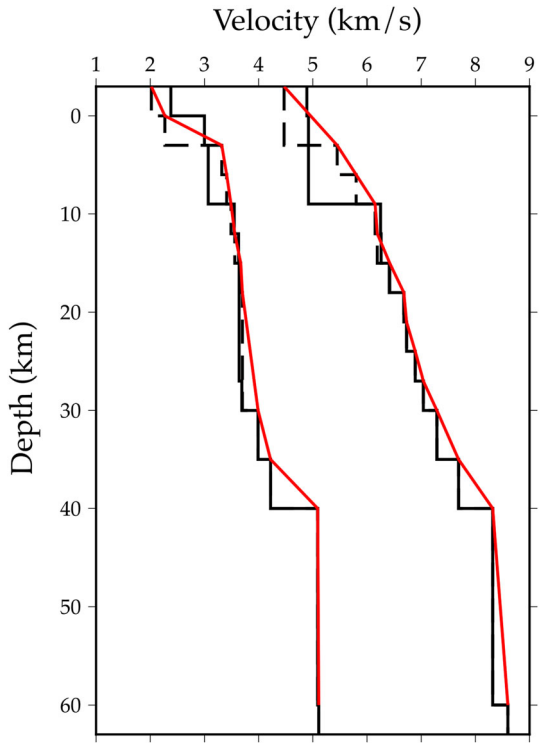

Figure 5. *P* and *S*waves velocity models. The black solid lines represent the model of Sielfeld et al. (2019), the black dashed lines show the velocity model updated for this study, and the red solid lines represent the gradient velocity layers that reduce the sharp discontinuity that occurs at 10 km depth.

location of the order of the HYPOINVERSE-2000 results). HypoDD works on the assumption that the distance between earthquake pairs is much less than the earthquake to station distance. With this in mind, relocation was applied aiming to maximize the number of events located, while keeping the separation between events in a small cluster. Each earthquake was paired with up to 30 neighbours located within 1.5 km, and each pair could have up to 24 linked arrivals. We run HypoDD in two sets of five iterations, taking initial locations from the Hypo2000 catalog and weighting the *S* phase data at 80% relative to *P* phases. Damping was evaluated and adjusted by cluster according to the resulting condition number (CND), making sure this was between 40 and 80 and that the absolute location difference of cluster centroids was within the average errors of the Hypo2000 catalog (Waldhauser & Ellsworth, 2000). We kept the residual threshold for the phase data (WRCT) and the maximum distance between phase pairs linked (WDCT) unconstrained for the first five iterations, letting the catalog improve the large-scale picture freely. The next five iterations are designed to reduce outliers, by reweighting WRCT and WDCT to 6 and 1.5 km, respectively. Due to the large number of earthquakes, we computed the relocation using the conjugate gradients method, LSQR (Waldhauser & Ellsworth, 2000). In total this resulted in 1,233 linked events, with an average offset of 0.029 km: 121,791 *P* wave traveltime pairs and 133,770 *S* wave traveltime pairs. The final relocated catalog includes 951 hypocenters and is shown in Figure 6a.

5. Spatial Distribution of Resistivity Anomalies and Seismicity

The resolution of conductivity anomalies discussed in this section has been validated with a series of robustness tests (see the supporting information). All anomalies within the model have proved to be robust through multiple sensitivity tests, with the exception of the low-resolution region below C1 (Figures 6 and 7, Sensitivity Tests 3 and 4).

Overall, two distinct resistivity domains can be distinguished in the study area: an eastern domain of low resistivity (<50 Ωm, Sensitivity Test 16) and a western domain of high resistivity (values between 500 and 10,000 Ωm, Sensitivity Tests 8 and 9). These two domains are best shown in Cross Sections WNW-1 and WNW-2 (Figure 7), both of which are perpendicular to the general trend of the resistivity contrast and trace of the EFFS. The conductive domain is aligned in a NNE volcanic arc-parallel orientation, as has been observed in comparable MT studies in the Southern and Central Andes (e.g., Díaz et al., 2015; Held et al., 2016; Hickson et al., 2011; Kapinos et al., 2016), and the majority of seismic hypocenters are located in the eastern domain, below and to the east of the EFFS. There is a distinct lack of seismicity in the western high resistivity domain (Figures 6 and 7), and almost all of the seismicity is located in the eastern footwall of the EFFS, and below 4 km depth (Figure 7, WNW-1 and WNW-2).

The eastern domain of low resistivity is segmented in the north-south orientation, populated by four distinct conductors (C1–C4, Sensitivity Tests 1, 6–8, 12, and 13) and two main seismic clusters (Cls1 and Cls2) (Figures 6 and 7). Seismic cluster Cls1 is elongated in a WNW direction and within a low conductivity (R1) region, adjacent to conductor C1 (e.g., Figure 7, Cross Sections NE-1, NE-2, NE-3, NW-5, and NW-6 compared to WNW-1) that is located NE of the Planchón-Peteroa volcanoes at a depth of 4–8 km. At 6 km (Figure 6d), the distinct WNW alignment of seismic cluster Cls1 extends for approximately 10 km length, aligning with an abrupt boundary between C1 and a WNW oriented resistive corridor (conductivity ranges 500–1,000 Ωm), R1 (Sensitivity Tests 10 and 11). This is interpreted to be an active ATF, as it shows similar characteristics to other ATF structures observed in different localities across the Andes. Namely, they are WNW trending, are discrete, blind, basement structures, and show spatial proximity to volcanoes, which can be emplaced at the intersection of the ATF and arc-parallel fault systems (Cembrano & Lara, 2009; Chernicoff et al., 2002; Lara et al., 2004; Roquer et al., 2017; Sielfeld et al., 2017;

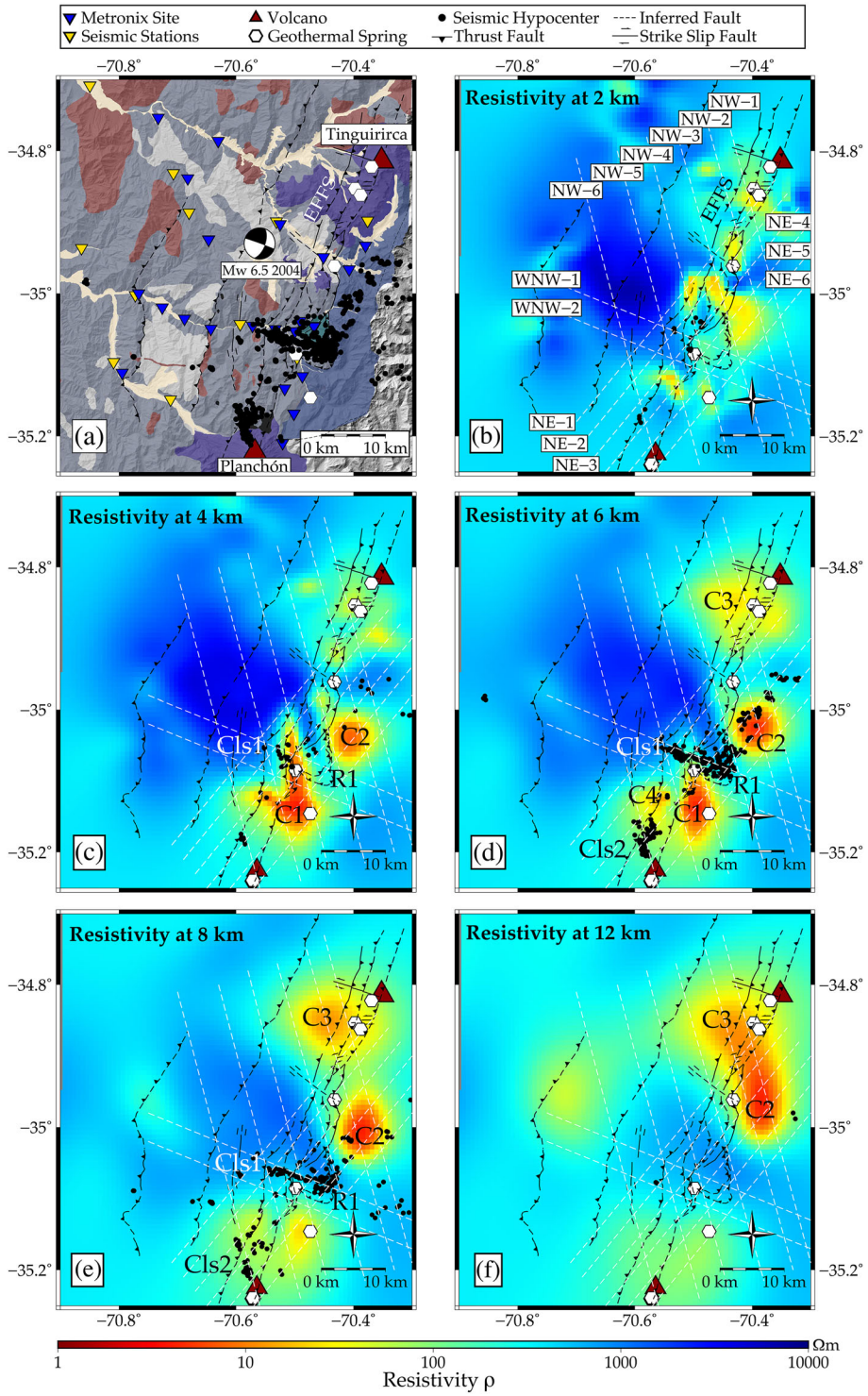

Figure 6. (a) Hypocenters located from the local seismic survey, projected onto a 12 m resolution DEM of the field study area along with important geological features (see Figure 2 for feature references). (b–f) Three-dimensional MT models plotted with seismic hypocenters at 2, 4, 6, 8, and 12 km depths, respectively, with seismicity projected within ±200 m at each depth. The EFFS, volcanoes, and geothermal springs are projected onto each map to indicate their surface localities. (a–f) White dashed lines indicate the location of the cross sections provided in Figure 7.

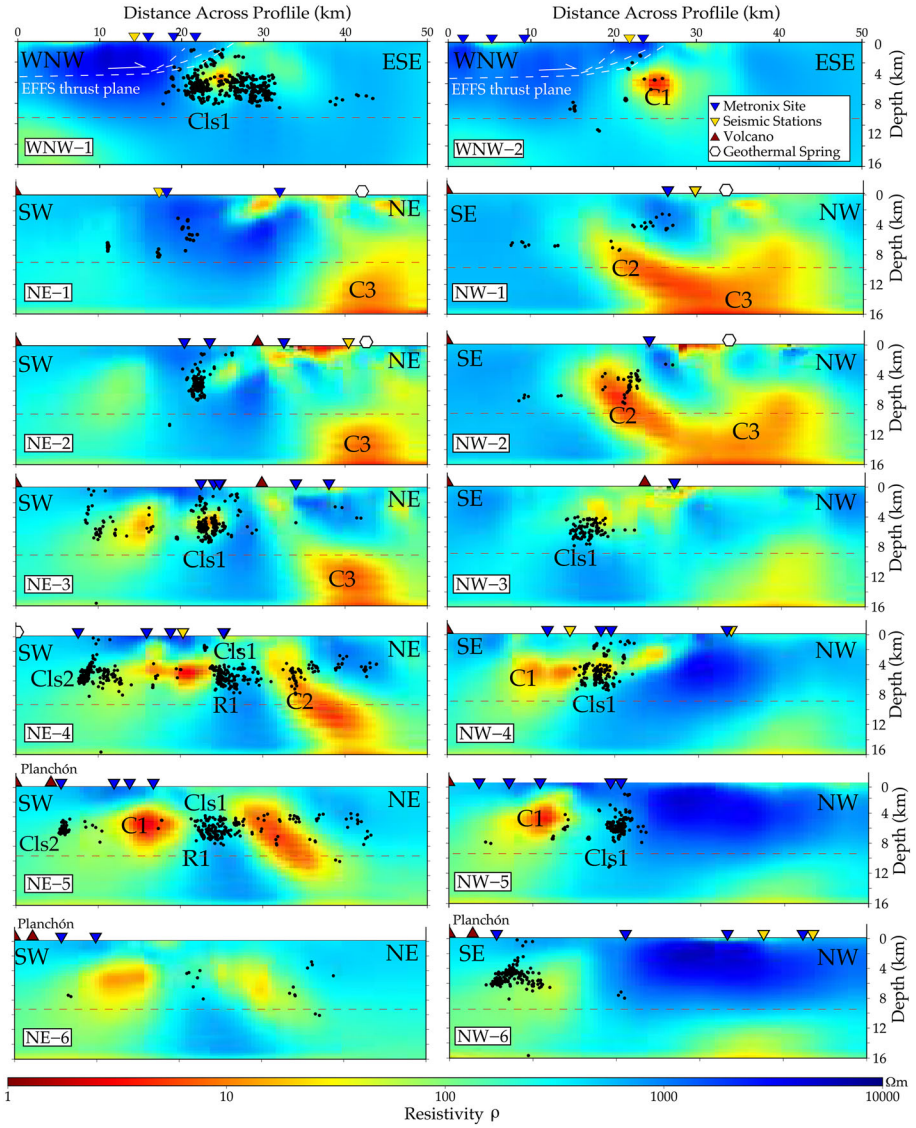

Figure 7. A set of 14 cross sections of the MT inversion model between 0 and 16 km, with seismic hypocenters projected within ±200 m lateral distance from the transect location. Also projected are MT and seismic station locations (blue and red triangles, respectively) that occur along the transects. See Figure 6 for profile locations. Conductive and seismic features described in the paper (C1, C2, C3, R1, Cls1, and Cls2) are labeled. Red dotted line at 9 km marks the depth boundary for seismic activity.

Stanton-Yonge et al., 2016; Veloso et al., 2019; Wrage et al., 2017). The majority of this WNW seismicity is located below 4 km, suggesting that the fault is located within the pre-Jurassic basement (Pavez et al., 2016). Furthermore, the seismicity is restricted to the footwall of the EFFS (Figures 6a and Figure 7, WNW-1). The primary correlation is therefore that the ATF separating the conductive anomalies is seismogenic (e.g., Clusters 1 and 2).

Seismic cluster Cls2 also occurs at a boundary between a conductive anomaly C4 and the more resistive region extending NE of the PPVC. The most southeastern cross sections, NE-5 and NE-6 (Figure 6), show the progressive disappearance of these features. Conductors C1 and C2 begin to diminish in strength toward the SW, and seismic clusters dissipate in NE-5, until there is little distinguishable conductive or seismogenic structure in NE-6. This may be a result of the model region extending outside the seismic and MT array. Seismic Cluster Cls2 is predominantly focused at 6–8 km depth in a region of low to intermediate resistivity (10–50 Ωm, C4 in Figures 6d and 6e, Sensitivity Test 18). The shape of this cluster is very similar to that of the

contour of the conductive anomaly, suggesting a connection between the two (Figure 6d). Furthermore, all seismic hypocenters occur within a 0–9 km depth range (see Figures 6 and 7).

Conductor C1, which extends NW of the PPVC, increases in conductivity northward from 75 Ωm (yellow) until it reaches a maximum of 5 Ωm (red) at the conductive boundary between C1 and R1 (Figures 6c and 6d, Sensitivity Test 13). This conductor is also contained between 4 and 8 km depth, above which there is a low conductivity cap (Figure 7, NE-4, Sensitivity Test 3).

Figure 6 shows a south-to-north increase in high-conductivity anomalies between 8 and 12 km of depth (Figures 6e and 6f, Sensitivity Tests 12 and 13) and an apparent connection between C2 and C3 at a 12 km depth (Figures 6e and 6f). A smaller conductor, C2 (conductivity ranges 5–50 Ωm), is present at a 4 km depth (Sensitivity Test 15) and connects to a deeper conductor, C3, at 10 km depth along an approximate northeastern dip. As MT has difficulty resolving the exact dip of the conductive anomalies, unless a very dense and localized survey is conducted, this dip angle can only be estimated. Conductor C3 is also connected through minor conductive branches with the shallow conductor correlated with the Termas del Flaco geothermal spring (NE-1, NE-2, NW-1, and NW-2, Figure 7), a known outflow spring of the Tinguiririca geothermal fields (Aravena et al., 2016; Benavente et al., 2016; Pavez et al., 2016). We interpret this to be the limb of an active hydrothermal system, sourced from a deeper magmatic body located beneath the Tinguiririca volcanic complex (C3).

In summary, seismic and conductive anomalies appear correlated in Figures 6 and 7. Both high conductivity anomalies and seismogenic zones occur east of the NNE oriented trend of the volcanic complexes and EFFS. There is also a prominent WNW oriented seismic cluster, Cls1, that occurs along an abrupt conductivity boundary (C1 and R1) of the same orientation that emerges at a 4 km depth and is strongest at a 6 km depth. Below 8 km, the region is aseismic, and a deeply rooted conductor (C3) emerges beneath the Tinguiririca complex at a 12 km depth that is connected to a smaller conductive limb that shallows toward the south (C2). Finally, a small seismic cluster (Cls2) shows coherent geometry and locality with a moderate conductor (C4) at 6–8 km of depth, slightly northwest of the Planchón-Peteroa edifices.

6. Discussion

Our results demonstrate that high-conductivity zones are located along the axis of the active volcanic chain (Figures 6b–6e). This suggests that the conductors are likely reservoirs of fluid and/or melt related to the active volcanic arc. As mentioned in section 3, the Andean volcanic arc has an anomalously high geothermal gradient and high concentrations of magmatically sourced fluids (Benavente et al., 2016; Giambiagi et al., 2019), both characteristics of which are associated with high conductivity (Ramos, 2010; Turienzo et al., 2012). This correlation of conductive anomalies located along the axis of the volcanic zone is observed in multiple comparable MT studies conducted in the Southern and Central Andes (e.g., Díaz et al., 2015; Held et al., 2016; Kapinos et al., 2016). While we have confidence in the spatial distribution of the conductors in the final MT model, there is some ambiguity as to the absolute conductivities of each feature. When a precise range of resistivity values for MT anomalies is defined, lithological properties of subsurface melt and crystalline mush in the Andean volcanic-arc setting can be resolved (Pommier, 2014), such as melt-fluid fractions (e.g., Cordell et al., 2018; Díaz et al., 2015) or melt viscosity and silica content (e.g., Comeau et al., 2016b). However, this analysis is best conducted if specific resistivity values and local rheological properties (e.g., melt composition) are well constrained, and isothermal profiles or the depth extent of hydrothermal fluid circulation domains are known. Due to the lack of these constraints local to the studied field area, resolving the lithological properties of conductive phases is not addressed in this study. Interpretation of the integrated seismic hypocenters and MT model is thus focused on discerning between melt or hydrothermal fluids, and their relationship to the seismic features that have been detected.

The east-west conductivity contrast that is bound by the EFFS fault is particularly apparent in Cross Sections WNW-1 and WNW-2 (Figure 7), on which the dip of the El Fierro fault plane has been projected using structural data from previous studies of this fault system (Giambiagi et al., 2019; Godoy et al., 1999). The WNW aligned seismicity cluster Cls1 and conductive anomaly C1 are contained within the footwall and east of the EFFS, while the domain west of the EFFS is relatively aseismic. We hypothesize that the EFFS plays a key role in compartmentalizing hydrothermal fluids to the east, as the fault zone acts as a barrier to cross-fault fluid migration and channels fault-parallel fluid flow to the surface from depth. This fault structure therefore

controls magmatic-derived hydrothermal fluid circulation and potentially associated seismogenic processes that occur east of the fault trace. This is supported by the exhumed alteration zone that occurs on the footwall of the exposed fault surface expression (Figures 3b and 3c) and how all geothermal springs and fumaroles are found along eastern strands of the fault system. The results from Pavez et al. (2016) (see section 3.2) indicate that the footwall of the EFFS facilitates the circulation of fluids sourced from an andesitic magma system below 6 km that underlies an active hydrothermal zone. Our data are consistent with this model, and conductors such as C2 and C3 likely represent such conduits. Furthermore, we believe that elevated pressures from these fluids may play a role in fault reactivation, as discussed in section 6.4.

6.1. Depth Extent of Seismicity and the Brittle-Ductile Transition

The majority of the earthquake hypocenters are located at a depth of 4–6 km, with more shallow events occurring closer to the EFFS. This suggests that the majority of seismicity is hosted within the pre-Jurassic basement rocks and the upper extent of seismicity is delineated by 4–5 km of thick Early Jurassic-Oligocene rocks (Pavez et al., 2016). At greater depths, there is a distinct seismicity boundary at around 9 km, below which little seismicity is apparent in any cross section. Such a seismicity boundary was observed in the regional-scale seismic survey conducted by Sielfeld et al. (2019) between latitudes 38°S and 40°S. Their results show an upper-crustal concave upward seismicity boundary that traverses the Andes. This boundary is considered concave as the seismic depth limit is 40 km at the plate margin, 20 km at the backarc in Argentina, and 10–12 km depth in the Principal Cordillera that is located between the margin and forearc (Lange et al., 2008; Legrand et al., 2011). It was suggested by Sielfeld et al. (2019) that this seismicity boundary marks an approximate isotherm of 340°C, based on preceding globally distributed borehole studies of quasi-plastic deformation in the crust (Suzuki et al., 2014), and the seismicity boundary delineates the brittle-ductile transition zone within the SVZ. The same interpretation of the seismicity boundary used by Sielfeld et al. (2019) and other comparable MT studies conducted in the southern Andes (e.g., Held et al., 2016) will be applied to the hypocenter results we have observed. We therefore interpret that the local seismicity boundary at 9–10 km depth in our area likely indicates the location of the brittle-ductile transition zone and marks an approximate 340°C isotherm.

6.2. Hydrothermal Fluids beneath the Planchón-Peteroa Volcano

Seismic Cluster Cls2 occurs at 4–8 km below and to the NW of Planchón-Peteroa (Figure 7, NE-4, NE-5, and NW-4) and is concurrent with a moderate conductivity anomaly, C4, of 10–50 Ωm, which is proximal to the major conductor C1. The conductive anomaly C4 is most prominent and shallowest at approximately 10 km NW of the volcanic complex, and seismicity spreads from the boundary of the conductors northwest from Planchón-Peteroa. Furthermore, given the low resolution in the MT model beneath C1, and as this conductor occurs at the edge of the MT array, it is possible that a more conductive medium occurs below or south of C1 and C4 that is not resolved by the model. With this ambiguity in mind, the following rationale provides supporting evidence that C1 and C4 are likely hydrothermal fluids with some deeper magmatic source. The precise location of the magmatic source of these fluids remains unknown due to the nonrobust regions of the model below and south of C1 and C4.

The source of C1 and C4 conductivity anomalies are interpreted to be the presence of fluids rather than magma or crystalline mush, based on previous studies of the Planchón-Peteroa volcanic activity that have occurred since 2011. It was determined by Aguilera et al. (2016) that the main phreatic eruption episode was driven by the release of deep magmatic gases as well as volatiles from a shallow hydrothermal reservoir. Tephra fall and vapor emissions contained no juvenile magmatic constituents and were mainly of hydrothermal origin. These volcanic products did, however, bear traces of deep oxidized magmatic fluids from a highly degassed (old) magmatic body, likely of dacitic or basaltic composition (Tassi et al., 2016). The results from the Tassi et al. (2016) study are supported by Benavente et al. (2016), who detected minor He signatures of a deep magmatic body within a dominantly hydrothermal regime below the volcano. It is therefore likely that the conductivity of C1 is largely sourced from the hydrothermal system, attested to by these studies. Furthermore, as the geothermal regime at depths between 0–8 km is colder than 340°C (section 6.1), and as the hydrothermal systems local to this region are established to be at approximately 250°C (Benavente et al., 2016), C1 and C4 are within the correct depth and temperature range to source these fluids.

Finally, an InSAR study conducted by Pritchard et al. (2013) detected the subsidence of the Southern Andean volcanic arc, including Tinguiririca, after the 2010 Mw 8.8 Maule earthquake. Results showed that the majority of ground deformation caused by the release of fluids from the subvolcanic hydrothermal systems does not occur directly beneath the volcanic edifice but is laterally offset from the main caldera. Additionally, the main geothermal outflow zone for Tinguiririca occurs at Termas del Flaco, which is located 15 km south of the main volcanic caldera (Pavez et al., 2016). Both studies provide supporting evidence that the main fluid reservoirs local to individual volcanoes show lateral offset at depth from the volcano. This supports our deduction that C1 and C4 are hydrothermal-magmatic reservoirs that are, respectively, offset NE and NW of the Planchón-Peteroa edifice.

Having attributed the conductor C1 to a resource of hydrothermal fluids, a likely explanation that the seismic cluster, Cls2, is induced by fluid migration or degassing of the volcano rather than the migration of magmatic material. This interpretation is supported by the recent phreatic eruptions that have characterized the volcano (section 3.1), the spatial proximity of the fluidized (conductive) zones proximal to the volcano (C1 and C4), and the evidence provided by Benavente et al. (2016) and Tassi et al. (2016) that the pluton within Planchón-Peteroa is cool and mature. Distinguishing whether the cluster is sourced from a redistribution of tectonic stress requires further spatial, temporal, and kinematic analysis of the seismic data. However, as the presence of fluids commonly contributes to seismogenic processes due to the reduction of effective stress local to the faulted structures (Cox, 2005, 2016), it is reasonable to expect that fluids are present within this cluster. Therefore, this seismic cluster is interpreted to be a fluid injection point, where episodic seismic release enhances fluid migration occurring within the volcano.

6.3. Deeply Rooted Conductor Beneath the Tinguiririca Volcano

The deeper feature, C3, located SW of the Tinguiririca Volcano that emerges at a 6 km depth is beyond the lateral boundaries of the MT station deployment. However, as MT measurements are capable of increased lateral coverage with increasing depth, and as this feature and its connectivity to the conductive feature C2 are shown to be robust within the inversion model (Sensitivity Tests 12, 13, and 15), interpretation is briefly explored. C3 is located SW of the Tinguiririca volcanic complex and is spatially associated with geothermal outflow springs at Termas del Flaco (refer to section 2.1) (Aravena et al., 2016; Clavero et al., 2011; Pavez et al., 2016; Pritchard et al., 2013). Its connectivity to the conductive limb C2, which emerges at a depth of 2 km, suggests that this shallower conductor is also a component of the active hydrothermal system that has been detected in this area. As trace elements of magmatic sources have been measured in the fumaroles and outflow springs associated with the Tinguiririca geothermal fields (Benavente et al., 2016), it is possible that these conductors are composed of both magmatic material and hydrothermal fluids.

Considering the dimensions and shallowness of C2, which extends from 2–12 km depth and has a volume of approximately 5 km^3, it is unlikely that this conductor consists of magma or crystalline mush, as a more pronounced volcanic feature would be situated above the conductor (Figures 6c–6f), as is observed in comparable studies based in the Andes (e.g., Comeau et al., 2016a; Cordell et al., 2018). Similar to Planchón-Peteroa, the temperature of the hydrothermal system is estimated to be 250°C between 2 and 6 km (Benavente et al., 2016), which suggests that a hydrothermal system is dominant at this depth range. This is supported by the correlating locality of the alteration zone that outcrops at the footwall of the El Fierro fault (Figures 2b and 3c), which occurs directly above Conductor C2 (Figure 6b). This suggests that fluid saturated zones have historically migrated toward the surface at this locality. It is possible that the C2 anomaly is not generated by hydrothermal fluids but by the conductive lithological phases of hydrothermally altered material. This does not conflict with the interpretation that C2 is an ascending limb of the hydrothermal system, but it implies that this circulation is extinct.

The deeper conductor C3 is a valid contender as a magmatic reservoir, considering its depth extent (8–16 km) and location directly beneath the Tinguiririca volcanic complex (Figures 6e and 6f). It was established by Pavez et al. (2016) using Vp/Vs ratios combined with geochemical analyses of fumarolic discharges that a magmatic body exists 8–12 km beneath the Tinguirirca volcanic edifice, which was determined to be a major source for fluid upflow zones that manifest between 2–6 km beneath the surface (section 3.2). The modeled MT results support this scenario; therefore, it is interpreted that C2 is the signature of zones of hydrothermal fluids migrating to the surface through brittle lithologies. This interpretation is supported

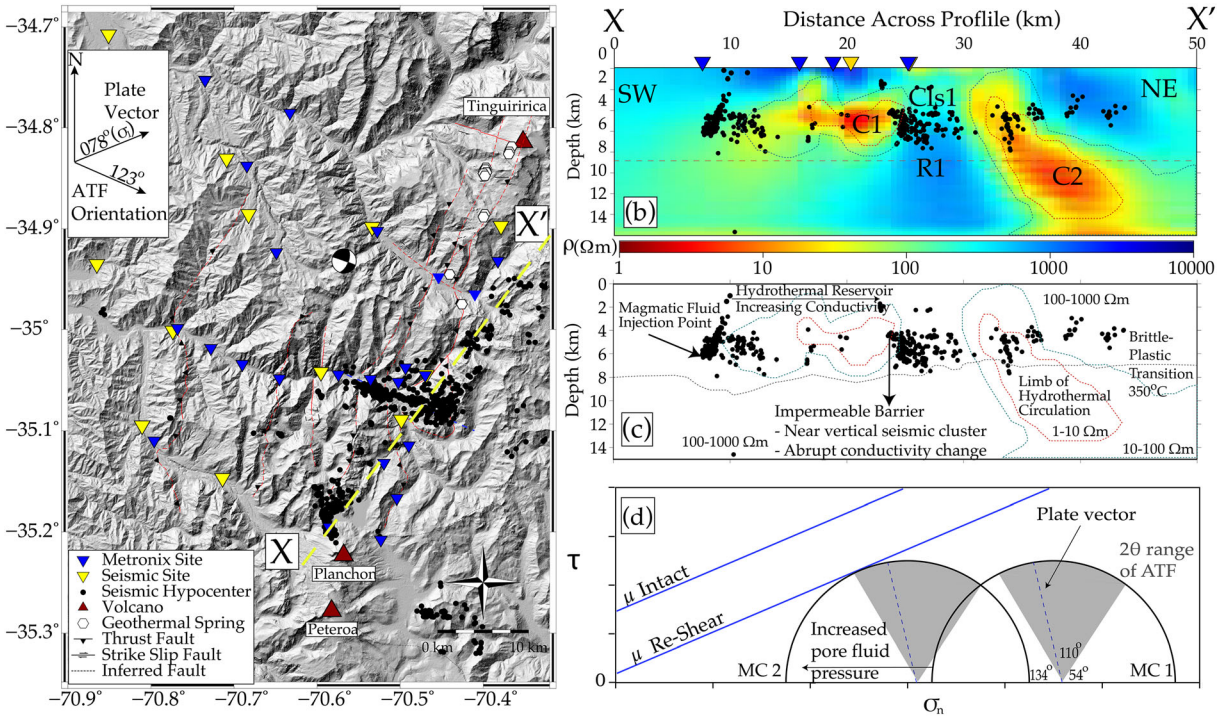

Figure 8. (a) All relative relocated seismic hypocenters from the local seismic survey projected onto a the 12.5 m resolution DEM of the field study area. The Teno earthquake moment tensor (Ekstrom et al., 2012), geothermal springs, Holocene volcano locations and associated units, station locations, and El Fierro Fault System are also shown. (b) NE oriented cross section of the MT model with seismic hypocenters projected within a 200 m lateral range of the cross section location; (c) schematic interpretation of the cross section in panel b. (d) A theoretical Mohr circle diagram illustrating the failure criterion envelopes for different stress regimes for fault reshear and the effect of pore fluid pressures on equivalent stress scenarios; each circle is marked as MC1-2. Grayed area represents range of quaternary stress orientations from Giambiagi et al. (2019).

by *Vp*/*Vs* ratios detected by Pavez et al. (2016), which identified shallow (0–3 km) Mesozoic sedimentary units (Figure 2b) as being highly fractured, thus acting as a high-permeability conduit for the migration of fluids from a deeper magma source to the surface. Conductor C3 is generated by crystalline mush or a magmatic body that is a major source of these fluids, as well as the geochemical traces of magma that have been detected in the geothermal outflow features local to this volcano (see section 3.2) (Benavente et al., 2016; Pavez et al., 2016). This model has also been proposed in other districts of the Andes, where a deep (10–14 km) conductor beneath a volcanic edifice is considered a magma reservoir (Comeau et al., 2016a; Díaz et al., 2015) and is the source for hydrothermal reservoirs that circulate in the shallow crust and generate shallower conductive anomalies (Díaz et al., 2015).

6.4. Reactivation of WNW ATF by Hydrothermal Fluids

The WNW trending cluster of Seismicity Cls1 shown in Figure 6d is interpreted as an ATF structure (Figure 8a). As discussed in section 2, these structures are considered discrete, reactivated, pre-Andean faults, which exert a fundamental control in the location and development of volcanic features. They are enigmatic as their orientation with respect to the regional stress field makes them unfavorable to transport magma through the lithosphere (Cembrano & Lara, 2009; Chernicoff et al., 2002; Piquer et al., 2019; Sielfeld et al., 2019). The seismicity of Cls1 does not extend to the surface nor is there any surface expression of the structure, which supports the hypothesis that the ATF domain is contained within the basement lithology, and that they are of Pre-Andean origin (Cembrano & Lara, 2009). Recent insights from isotope geochemistry show that the geochemical signatures of water emerged from ATF have high degrees of crustal contamination (Tardani et al., 2016), signatures of magmatic vaporization of cold water recharge (Sanchez et al., 2013), and a longer crustal residence time in the ATF domain relative to major NNE trending fault systems (Wrage et al., 2017). Structural and mineralogical analyses of the faults have shown that fluid pressures between >85% and 98% of lithostatic stress can be required to trigger hybrid (extension plus shear) mode of failure (Roquer et al., 2017). It is therefore likely that fluid migration through these systems occurs in moments

of seismic activity and conversely host hydrothermal reservoirs due to the entrapment of fluids during interseismic periods (Roquer et al., 2017; Veloso et al., 2019). Finally, rare outcrops of the ATF are characterized by multiple fault cores and dense vein networks within a wide damage zone, which prevent cross-fault fluid flow due to their low permeability (Lara et al., 2004; Perez-Flores et al., 2016).

Seismic Cluster Cls1 follows the distinct conductivity contrast of Conductor C1 and Resistor R1 (see section 5). The occurrence of seismogenic features at abrupt conductive boundaries has been observed in comparable MT and seismic studies conducted along the San Andreas Fault, Taupo Volcanic Zone, and an intraplate setting in central Botswana (Avdeeva et al., 2015; Becken et al., 2011; Ingham et al., 2009). These studies suggest that earthquakes tend to occur adjacent to zones of high conductivity, either at the boundaries or within the regions of the neighboring resistive rock. This occurrence is due to the migration of fluids into a permeable, mechanically weak zone (characterized by low resistivity) adjacent to a less permeable, mechanically strong zone (characterized by high resistivity), causing the accumulation of high fluid pressures and subsequent brittle rock failure (Becken et al., 2011; Cox, 2005). This process can occur in fault zones, where impermeable fault cores prevent cross-fault fluid flow causing the increase of local fluid pressures, while the permeable fracture mesh aligned parallel to the fault core enhances fault-parallel fluid flow (Faulkner et al., 2010; Hoffman-Rothe et al., 2004; Rowland & Sibson, 2004; Sibson, 1996).

The predominance of seismicity at abrupt conductivity contrasts suggests that fluid accumulation can locally trigger reactivation of preexisting ATF structures. It is interpreted that the smaller seismic cluster that resides beneath the Planchón-Peteroa system (Cls2) is a channel for volcanically sourced fluids that accumulate in a hydrothermal reservoir north of the complex. This reservoir is the source of the anomaly C1, which increases in conductivity northward until it reaches a maximum at the conductive boundary between C1 and R1, and the seismic cloud, Cls1. We illustrate the state of stress using a Mohr-Coulomb failure diagram (Figure 8d), which is drawn on the assumption that the ATF are inherent, WNW oriented, pre-Andean structures with a strike of approximately 110° (estimated from the 2004 Mw 6.5 Teno earthquake focal mechanism; Ekstrom et al., 2012), with no cohesive strength (Sibson, 1985). These faults activate as sinistral-strike slip and reverse modes under the current stress regime (Stanton-Yonge et al., 2016), evident from the 2004 Mw 6.5 focal mechanism (Figure 8a) and observations from similar ATF structures south of the studied area (Sielfeld et al., 2019). A simple Andersonian relationship is assumed (Anderson, 1942), where σ_2 is along the vertical axis and σ_1 and σ_3 are in a horizontal plane and that σ_1 ranges between N65°E and N88°E, considering the angle of convergence and the associated possible orientations of the instantaneous shortening axes in a transpressional margin (Perez-Flores et al., 2016; Teyssier et al., 1995). The angle between σ_1 and the fault plane is approximately between 58° and 35°, showing that it is not optimally oriented for reactivation. Therefore, increasing fluid pressure could induce reactivation of the fault by decreasing the effective normal stress. In the absence of local measurements of stress orientations, there is uncertainty as to whether the stress field includes strain partitioning across the transpressional plate margin (e.g., Teyssier et al., 1995; Tikoff & Teyssier, 1994) and/or mechanical interaction between faults across the volcanic arc (e.g., Stanton-Yonge et al., 2016). Future studies will be conducted using our seismic catalog to determine fault plane solutions and conduct a kinematic analysis of fault-slip data and thus constrain local stress orientations.

It should be noted that a small protrusion of C1 occurs at 4 km depth above Cls1, observable in Figure 6c and Cross Sections NW-3 and NW-4. This conductor may represent fluid migration; however, as it does not cross the seismic cluster region, we regard this feature to support our argument that the observed ATF is impermeable to fluid flow.

6.5. Conceptual Model of Hydrothermal System

Figure 9a shows a presents a 3D view of the final model, and Figure 9b shows a schematic interpretation of the features observed from this perspective. It is interpreted that the resistive, seismogenic structure considered to be an ATF interacts with the deeply rooted conductor beneath Tinguiririca. We interpret Conductor C2 to be the limb of a hydrothermal system sourced from a magmatic origin identified with the deeper conductor, C3 (section 6.3). This limb channels fluids toward the surface along the fault plane of the ATF. Unlike the hydrothermal reservoir on the southern region (C1), which results in overpressure and drives fault reactivation (section 6), the region surrounding Conductor C2 shows no dense seismic clusters. We suggest that Conductor C2 is a zone of permeable, saturated rock within which the pore fluid pressure is in

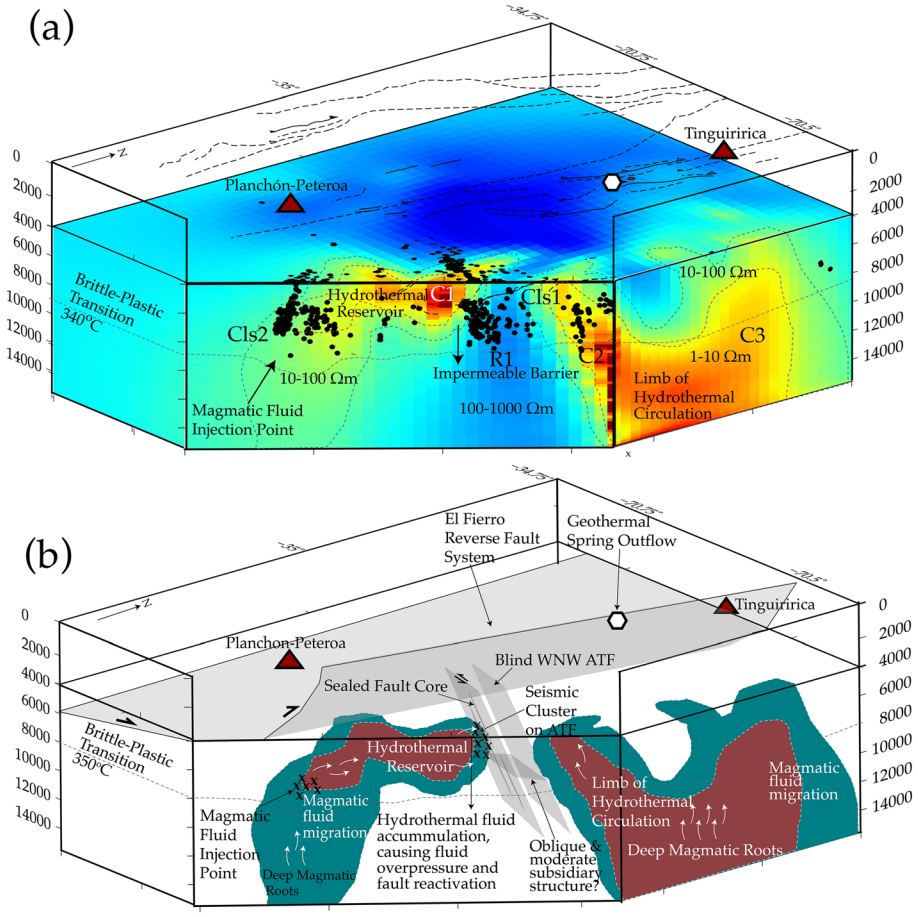

Figure 9. (a) Three-dimensional presentation of the conductivity model at 4 km depth along the horizontal plane and Cross Sections NE-4 and NW-2 (Figure 7) from 4–16 km depth placed at accurate transect locations. Seismic hypocenters are shown along these planes to illustrate their distribution in 3D, with all seismicity projected onto the 4 km horizontal plane to highlight the NW orientation of Cls1. Annotations highlight the interpretations discussed in sections 5–7, and the EFFS and volcanic complexes are projected at 0 km depth to contextualize their locality at the surface; (b) a schematic interpretation of the model results illustrates the hydrovolcanic system that is proposed for this area (section 7).

excess of hydrostatic pressure. This hypothesis is supported by the presence of significant geothermal outflow springs of deep-sourced fluids, such as those found at Termas del Flaco, which accumulate in the geothermal fields associated with the Tinguiririca volcanic complex (Aravena et al., 2016; Benavente et al., 2016; Giambiagi et al., 2019; Pavez et al., 2016; Pritchard et al., 2013). Conversely, the Planchón-Peteroa reservoir has a resistive cap that extends to 4 km depth. The presence of capping structures in the ATF domain has been previously hypothesized as a control on their rupture cycle (Roquer et al., 2017). The conductor C1 is therefore contained at depth of 4 km by the resistive cap, is northwardly bound by the ATF of a WNW orientation, and is westward bound by the EFFS of a NNE orientation. The conductor therefore occurs at the intersection of these two fault structures.

This tectonohydrothermal environment has been observed in different regions of the Andes, where the intersections of major NNE thrust faults and ATF are hosts to giant ore-porphyry deposits (Figure 1) (e.g., Chernicoff et al., 2002; Cox, 2005; Curewitz & Karson, 1997; Piquer et al., 2019; Rowland & Simmons, 2012; Sillitoe, 1997; Veloso et al., 2019). These points of intersection have also been deduced to impact geothermal reservoir development (Perez-Flores et al., 2017; Sanchez et al., 2013). Therefore, this study provides a site-specific example of how the intersections of these major, margin-parallel thrust fault systems and ATF are hosts to magmatically sourced hydrothermal reservoirs at 4–8 km depths.

7. Conclusions

Results from this combined MT and seismic study can be summarized with six distinct observations:

1. An eastern conductive and western resistive domain is correlated with a seismicity boundary that occurs across all depths, following the trend of the volcanic arc and NNE trending EFFS. This is interpreted to be the signature of magmatic sources beneath the volcanic arc. These domains are characterized by higher conductivities than the surrounding regions due to high temperatures and the concentration of volcanically derived fluids. We also conclude that these conductive and seismic signatures are bounded by the footwall of the EFFS, due to the low permeability fault cores that prevent cross-fault fluid migration.
2. A WNW trending seismogenic fault is identified on an abrupt electrical conductivity contrast that occurs between 4 and 8 km of depth. We interpret this seismogenic feature to be a reactivated ATF, and the electrically conductive domain to be a hydrothermal reservoir. We conclude that the impermeable fault core of the ATF prevents cross-fault fluid flow, therefore, the accumulation of fluids increases pore fluid pressures and favors fault reactivation despite its unfavorable orientation relative to the regional stress field.
3. A deep conductor beneath the Tinguiririca volcanic complex emerges at an 8 km depth and increases in volume and conductivity with increasing depth. It shows some connection to the surface with minor conductive branches that show spatial coherence with the major geothermal outflow spring Termas del Flaco. This high-conductivity anomaly is interpreted to be a deep volcanic root that sources the geothermal springs and fumaroles observed at the base and edifice of the Tinguiririca volcanic complex, as well as the geothermal fields that have been thoroughly prospected in this area.
4. There is a minor seismic cluster and conductor beneath the PPVC that is highly concentrated at 8 km depths. These volcanoes have been intermittently on yellow alert for ash emission and degassing events since 2011, suggesting this seismicity is related to the release of volcanic derived fluids and volatiles into the shallower crust, recharging the hydrothermal reservoir above.
5. There is a distinct aseismic boundary at 8–10 km of depth, below which there is no seismicity. This is interpreted to be the brittle-ductile transition zone, and a definitive 340°C isotherm that is observed across the Andean volcanic margin.
6. The hydrothermal reservoir that extends NW from the Planchón-Peteroa volcano is contained at the intersection of the NNE trending EFFS, the WNW trending ATF, and a resistive cap that extends to a depth of 4 km. These results support preceding evidence that hydrothermal reservoirs and ore deposits occur at intersections of these fault systems at multiple locations across the Andes.

This combined seismic and MT study provides a site-specific example of how an ATF interacts with local volcanic and hydrothermal systems. In this case, it is proposed that the ATF fails despite its non-optimal orientation with respect to the regional stress field due to the influence of high pore fluid pressures acting on the fault plane. These results contribute to our understanding of the mechanical and architectural relationship of the ATF and NNE trending, margin parallel fault systems, and their control on the spatial development of hydrothermal reservoirs. These conclusions may be applicable to other occurrences of intersecting ATF and NNE trending fault systems in the Andean SVZ.

Acknowledgments

Funding was provided by NERC Grant NE/M004716/1 to T. M. M. and an RTSG to R. K. P. and A. S. M. G. from the London NERC DTP, with financial help from the Chilean National Fund for Scientific and Technological Development (FONDECYT: Grant Number 1141139), and the Canadian Centennial Scholarship Fund (CCSF), to whom we express our sincerest gratitude for making the study possible. We are very grateful to all of those involved in the field work, through the allotment of land to deploy our instruments, and the assistance in the logistics and/or labor of the deployment. For their incredible contribution to this effort, we would like to give special thanks to Mariel Castillo, Matias Cavieres, Manuel Dorr, Victorino Arauco, Gerd Seilfeld, Elias Lira, Nati and Mati Mohring, Jac Thomas, Emily Franklin, Pamela Prez-Flores, James Strachan, Daniela Balladares, Steve Boon, John Browning, Ronny Figueroa, and Javiera Ruz. Broadband MT equipment was kindly provided by PUC and Universidad de Chile. Many thanks to Anna Kelbert for her support during the archival process and to Jared Peacock for his assistance in the use of MTPy (Peacock et al., 2019).

Data Availability Statement

All MT transfer functions are publicly available on the IRIS EMTF archive (Kelbert et al., 2011) (listed under http://10.17611/DP/EMTF/UCL/CHILEMT). The UK seismic instruments and data management facilities were provided under Loan Number 1073 by SEIS-UK at the University of Leicester. The facilities of SEIS-UK are supported by the NERC under Agreement R8/H10/64. All seismic data are archived at IRIS (https://www.fdsn.org/networks/detail/6A_2017/). QuakeMigrate software is hosted in GitHub platform (https://github.com/QuakeMigrate/QuakeMigrate).

References

Acocella, V., Gioncada, A., Omarini, R., Riller, U., Mazzuoli, R., & Vezzoli, L. (2011). Tectonomagmatic characteristics of the back-arc portion of the Calama-Olacapato-El Toro Fault Zone, Central Andes. *Tectonics*, *30*, TC3005. https://doi.org/10.1029/2010TC002854

Aguilera, F., Benavente, Ó., Gutiérrez, F., Romero, J., Saltori, O., González, R., et al. (2016). Eruptive activity of planchón-peteroa volcano for period 2010–2011, southern andean volcanic zone, Chile. *Andean Geology*, *43*, 20–46.

Anderson, E. M. (1942). *The dynamics of faulting and dyke formation with applications to Britain* (p. 191). Edinburgh: Oliver and Boyd.

Angermann, D., Klotz, J., & Reigber, C. (1999). Space-geodetic estimation of the Nazca-South America Euler vector. *Earth and Planetary Science Letters*, *171*, 329–334.

Aravena, D., Munoz, M., Morata, D., Lahsen, A., Parada, M. A., & Dobson, P. (2016). Assessment of high enthalpy geothermal resources and promising areas of Chile. *Geothermics*, *59*, 1–13.

Aron, F., Cembrano, J., Astudillo, F., Allmendinger, R. W., & Arancibia, G. (2015). Constructing forearc architecture over megathrust seismic cycles: Geological snapshots from the Maule earthquake region, Chile. *Geological Society of America Bulletin*, *127*, 464–479.

Avdeev, D., & Avdeeva, A. (2009). 3D magnetotelluric inversion using a limited-memory quasi-Newton optimization. *Geophysics*, *74*, F45–F57.

Avdeev, D. B. (2005). Three-dimensional electromagnetic modelling and inversion from theory to application. *Surveys in Geophysics*, *26*, 767–799.

Avdeeva, A., Moorkamp, M., Avdeev, D., Jegen, M., & Miensopust, M. (2015). Three-dimensional inversion of magnetotelluric impedance tensor data and full distortion matrix. *Geophysical Journal International*, *202*(1), 464–481. https://doi.org/10.1093/gji/ggv144

Becken, M., & Ritter, O. (2012). Magnetotelluric studies at the San Andreas Fault zone: Implications for the role of fluids. *Surveys in Geophysics*, *33*, 65–105.

Becken, M., Ritter, O., Bedrosian, P. A., & Weckmann, U. (2011). Correlation between deep fluids, tremor and creep along the central San Andreas Fault. *Nature*, *480*, 87–U248.

Benavente, O., Tassi, F., Reich, M., Aguilera, F., Capecchiacci, F., Gutierrez, F., et al. (2016). Chemical and isotopic features of cold and thermal fluids discharged in the Southern Volcanic Zone between 32.5°S and 36°S: Insights into the physical and chemical processes controlling fluid geochemistry in geothermal systems of Central Chile. *Chemical Geology*, *420*, 97–113.

Bertrand, E., Caldwell, T., Hill, G., Wallin, E., Bennie, S., Cozens, N., et al. (2012). Magnetotelluric imaging of upper-crustal convection plumes beneath the Taupo Volcanic Zone, New Zealand. *Geophysical Research Letters*, *39*, L02304. https://doi.org/10.1029/2011GL050177

Bibby, H., Caldwell, T., & Brown, C. (2005). Determinable and non-determinable parameters of galvanic distortion in magnetotellurics. *Geophysical Journal International*, *163*(3), 915–930. https://doi.org/10.1111/j.1365-246X.2005.02779.x

Bonali, F. L., Tibaldi, A., Corazzato, C., Tormey, D. R., & Lara, L. E. (2013). Quantifying the effect of large earthquakes in promoting eruptions due to stress changes on magma pathway: The Chile case. *Tectonophysics*, *583*, 54–67. https://doi.org/10.1016/j.tecto.2012.10.025

Caine, J. S., Evans, J. P., & Forster, C. B. (1996). Fault zone architecture and permeability structure. *Geology*, *24*(11), 1025–1028. https://doi.org/10.1130/0091-7613(1996)024<1025:FZAAPS>2.3.CO;2

Cembrano, J., & Lara, L. (2009). The link between volcanism and tectonics in the southern volcanic zone of the Chilean Andes: A review. *Tectonophysics*, *471*(1–2), 96–113. https://doi.org/10.1016/j.tecto.2009.02.038

Charrier, R., Baeza, O., Elgueta, S., Flynn, J. J., Gans, P., Kay, S. M., et al. (2002). Evidence for Cenozoic extensional basin development and tectonic inversion south of the flat-slab segment, southern Central Andes, Chile (33 degrees-36 degrees SL). *Journal of South American Earth Sciences*, *15*(1), 117–139. https://doi.org/10.1016/S0895-9811(02)00009-3

Charrier, R., Pinto, L., & Rodríguez, M. P. (2007). *Tectonostratigraphic evolution of the Andean Orogen in Chile* (pp. 21–114). London: Geological Society Special Publication.

Charrier, R., Ramos, V. A., Tapia, F., & Sagripanti, L. (2015). Tectono-stratigraphic evolution of the Andean Orogen between 31 and 37°S (Chile and Western Argentina). *Geological Society, London, Special Publications*, *399*(1), 13–61. https://doi.org/10.1144/SP399.20

Chave, A. D. (1989). BIRRP: Bounded influence, remote reference processing. *Journal of Geophysical Research*, *94*(B10), 14,215–14,225. https://doi.org/10.1029/JB094iB10p14215

Chave, A. D., & Jones, A. G. (2012). *The magnetotelluric method: Theory and practice*. In A. D. Chave & A. G. Jones (Eds.). Cambridge University Press.

Chave, A. D., & Thomson, D. J. (2003). A bounded influence regression estimator based on the statistics of the hat matrix. *Journal of the Royal Statistical Society: Series C: Applied Statistics*, *52*, 307–322.

Chernicoff, C. J., Richards, J. P., & Zappettini, E. O. (2002). Crustal lineament control on magmatism and mineralization in northwestern Argentina: Geological, geophysical, and remote sensing evidence. *Ore Geology Reviews*, *21*, 127–155.

Clavero, J., Pineda, G., Mayorga, C., Giavelli, A., Aguirre, I., Simmons, S., et al. (2011). Geological, geochemical, geophysical and first drilling data from Tinguiririca geothermal area, central Chile. *Geothermal Resources Council Transactions*, *35*, 731–734.

Comeau, M. J., Unsworth, M. J., & Cordell, D. (2016a). New constraints on the magma distribution and composition beneath Volcan Uturuncu and the southern Bolivian Altiplano from magnetotelluric data. *Geosphere*, *12*, 1391–1421.

Comeau, M. J., Unsworth, M. J., & Cordell, D. (2016b). New constraints on the magma distribution and composition beneath Volcán Uturuncu and the southern Bolivian Altiplano from magnetotelluric data. *Geosphere*, *12*, 1391–1421.

Cordell, D., Unsworth, M. J., & Díaz, D. (2018). Imaging the Laguna del Maule Volcanic Field, central Chile using magnetotellurics: Evidence for crustal melt regions laterally-offset from surface vents and lava flows. *Earth and Planetary Science Letters*, *488*, 168–180.

Cox, S. F. (2005). Coupling between deformation, fluid pressures, and fluid flow in ore-producing hydrothermal systems at depth in the crust. *Economic Geology*, *100*, 39–75.

Cox, S. F. (2010). The application of failure mode diagrams for exploring the roles of fluid pressure and stress states in controlling styles of fracture-controlled permeability enhancement in faults and shear zones. *Geofluids*, *10*, 217–233.

Cox, S. F. (2016). Injection-driven swarm seismicity and permeability enhancement: Implications for the dynamics of hydrothermal ore systems in high fluid-flux, overpressured faulting regimes-an invited paper. *Economic Geology*, *111*, 559–587.

Curewitz, D., & Karson, J. A. (1997). Structural settings of hydrothermal outflow: Fracture permeability maintained by fault propagation and interaction. *Journal of Volcanology and Geothermal Research*, *79*, 149–168.

Díaz, D., Heise, W., & Zamudio, F. (2015). Three-dimensional resistivity image of the magmatic system beneath Lastarria volcano and evidence for magmatic intrusion in the back arc (northern Chile). *Geophysical Research Letters*, *42*, 5212–5218. https://doi.org/10.1002/2015GL064426

Drew, J., White, R. S., Tilmann, F., & Tarasewicz, J. (2013). Coalescence microseismic mapping. *Geophysical Journal International*, *195*, 1773–1785.

Droguett, B., Morata, D., Clavero, J., Pineda, G., Morales-Ruano, S., & Carrillo-Rosúa, J. (2012). *Mineralogía de alteración en el pozo Pte-1, campo geotermal Tinguiririca*. Antofagasta, Chile: XIII Geological Congress of Chile.

Ekstrom, G., Nettles, M., & Dziewonski, A. M. (2012). The global CMT project 2004–2010: Centroid-moment tensors for 13,017 earthquakes. *Physics of the Earth and Planetary Interiors*, *200*, 1–9.

Farias, M., Comte, D., Charrier, R., Martinod, J., David, C., Tassara, A., et al. (2010). Crustal-scale structural architecture in central Chile based on seismicity and surface geology: Implications for Andean mountain building. *Tectonics*, *29*, TC3006. https://doi.org/10.1029/2009TC002480

Faulkner, D. R., Jackson, C. A. L., Lunn, R. J., Schlische, R. W., Shipton, Z. K., Wibberley, C. A. J., & Withjack, M. O. (2010). A review of recent developments concerning the structure, mechanics and fluid flow properties of fault zones. *Journal of Structural Geology*, *32*, 1557–1575.

Giambiagi, L., Alvarez, P., Spagnotto, S., Godoy, E., Lossada, A., Mescua, J., et al. (2019). Geomechanical model for a seismically active geothermal field: Insights from the Tinguiririca volcanic-hydrothermal system. *Geoscience Frontiers*, *10*, 2117–2133.

Godoy, E., & Lara, L. (1994). Segmentación estructural andina a los 33–34: nuevos datos en la Cordillera Principal, Congreso Geológico Chileno (pp. 1344–1348).

Godoy, E., Yanez, G., & Vera, E. (1999). Inversion of an Oligocene volcano-tectonic basin and uplifting of its superimposed Miocene magmatic arc in the Chilean Central Andes: First seismic and gravity evidences. *Tectonophysics*, *306*, 217–236.

Gow, P. A., & Walshe, J. L. (2005). The role of preexisting geologic architecture in the formation of giant porphyry-related Cu ± Au deposits: Examples from New Guinea and Chile. *Economic Geology*, *100*, 819–833.

GVP (2020). Global Volcanism Program, Smithsonian Institution.

Hammond, J. O. S., Garzon, A. S. D. L. M., Pearce, R., Marshall, N., Mitchell, T., & Cembrano, J. (2017). Teno Valley Seismic Network [Data set]. International Federation of Digital Seismograph Networks.

Hedenquist, J. W., & Lowenstern, J. B. (1994). The role of magmas in the formation of hydrothermal ore-deposits. *Nature*, *370*, 519–527.

Held, S., Schill, E., Pavez, M., Diaz, D., Munoz, G., Morata, D., & Kohl, T. (2016). Resistivity distribution from mid-crustal conductor to near-surface across the 1200 km long Liquine-Ofqui Fault System, southern Chile. *Geophysical Journal International*, *207*, 1387–1400.

Hickson, C., Ferraris, F., Rodriquez, C., Sielfeld, G., Henriquez, R., Gislason, T., et al. (2011). The Mariposa Geothermal System, Chile. *Geothermal Resources Council Transactions*, *35*, 817–825.

Hoffman-Rothe, A., Ritter, O., & Janssen, C. (2004). Correlation of electrical conductivity and structural damage at a major strike-slip fault in northern Chile. *Journal of Geophysical Research*, *109*, B10101. https://doi.org/10.1029/2004JB003030

Ingham, M. R., Bibby, H. M., Heise, W., Jones, K. A., Cairns, P., Dravitzki, S., et al. (2009). A magnetotelluric study of Mount Ruapehu volcano, New Zealand. *Geophysical Journal International*, *179*, 887–904.

Kapinos, G., Montahaei, M., Meqbel, N., & Brasse, H. (2016). Three-dimensional electrical resistivity image of the south-central Chilean subduction zone. *Tectonophysics*, *666*, 76–89.

Katz, H. (1971). Continental margin in Chile—Is tectonic style compressional or extensional? *AAPG Bulletin*, *55*, 1753–1758.

Kelbert, A., Egbert, G., & Schultz, A. (2011). IRIS DMC data services products: EMTF, the magnetotelluric transfer functions. National Geoelectromagnetic Facility Technical Report.

Kissling, E., Ellsworth, W. L., Eberhartphillips, D., & Kradolfer, U. (1994). Initial reference models in local earthquake tomography. *Journal of Geophysical Research*, *99*(B10), 19635–19646. https://doi.org/10.1029/93JB03138

Klein, F. W. (2002). User's guide to HYPOINVERSE-2000, a Fortran program to solve for earthquake locations and magnitudes. US Geological Survey.

Lange, D., Cembrano, J., Rietbrock, A., Haberland, C., Dahm, T., & Bataille, K. (2008). First seismic record for intra-arc strike-slip tectonics along the Liquine-Ofqui fault zone at the obliquely convergent plate margin of the southern Andes. *Tectonophysics*, *455*, 14–24.

Lara, L., Naranjo, J., & Moreno, H. (2004). Rhyodacitic fissure eruption in Southern Andes (Cordón Caulle; 40.5 S) after the 1960 (Mw: 9.5) Chilean earthquake: A structural interpretation. *Journal of Volcanology and Geothermal Research*, *138*, 127–138.

Lara, L. E., Lavenu, A., Cembrano, J., & Rodriguez, C. (2006). Structural controls of volcanism in transversal chains: Resheared faults and neotectonics in the Cordon Caulle-Puyehue area (40.5°S), Southern Andes. *Journal of Volcanology and Geothermal Research*, *158*, 70–86.

Legrand, D., Barrientos, S., Bataille, K., Cembrano, J., & Pavez, A. (2011). The fluid-driven tectonic swarm of Aysen Fjord, Chile (2007) associated with two earthquakes (Mw = 6.1 and Mw = 6.2) within the Liquine-Ofqui Fault Zone. *Continental Shelf Research*, *31*, 154–161.

Lira Martínez, E. S. (2011). Estudio de sismicidad, tomografía sísmica y modelo de física de rocas: Potencial sistema geotermal asociado al complejo volcánico Tinguiririca.

Melnick, D., Bookhagen, B., Strecker, M. R., & Echtler, H. P. (2009). Segmentation of megathrust rupture zones from fore-arc deformation patterns over hundreds to millions of years, Arauco peninsula, Chile. *Journal of Geophysical Research*, *114*, B01407. https://doi.org/10.1029/2008JB005788

Melnick, D., & Echtler, H. P. (2006). Morphotectonic and geologic digital map compilations of the south-central Andes (36°–42°S). *Frontiers in Earth Science Series* (pp. 565–568). Berlin, Heidelberg: Spinger. https://doi.org/10.1007/978-3-540-48684-8_30

Mescua, J. F., Giambiagi, L. B., & Ramos, V. A. (2013). Late Cretaceous uplift in the Malargüe fold-and-thrust belt (35°S), southern Central Andes of Argentina and Chile. *Andean Geology*, *40*, 102–116.

Micklethwaite, S., Sheldon, H. A., & Baker, T. (2010). Active fault and shear processes and their implications for mineral deposit formation and discovery. *Journal of Structural Geology*, *32*, 151–165.

Miensopust, M. P., Queralt, P., Jones, A. G., & Modellers, D. M. (2013). Magnetotelluric 3-D inversion—A review of two successful workshops on forward and inversion code testing and comparison. *Geophysical Journal International*, *193*, 1216–1238. https://doi.org/10.1093/gji/ggt066

Moorkamp, M., Jones, A. G., & Fishwick, S. (2010). Joint inversion of receiver functions, surface wave dispersion, and magnetotelluric data. *Journal of Geophysical Research*, *115*, B04318. https://doi.org/10.1029/2009JB006369

Moreno, H. (1976). The upper Cenozoic volcanism in the Andes of southern Chile (From 40 00′ to 41 30′ SL), Proc IAVCEI Symposium on Andean and Antarctic Volcanology Problems, pp. 143–171.

Mpodozis, C., & Cornejo, P. (2012). Cenozoic tectonics and porphyry copper systems of the Chilean Andes. Soc Econ Geol Spec P, 329–360.

Mpodozis, C., Ramos, V., Ericksen, G., Canas Pinochet, M., & Reinemund, J. (1989). Geology of the Andes and its relation to hydrocarbon and mineral resources, pp. 59–90.

Nakamura, K. (1977). Volcanos as possible indicators of tectonic stress orientation—Principle and proposal. *Journal of Volcanology and Geothermal Research*, *2*, 1–16.

Núñez Tapia, R. C. (2018). Procesos de transporte de fluidos hidrotermales a lo largo de un sistema de fallas: Geología estructural y modelamiento numérico con elementos de borde.

Palsar, A. (2011). Jaxa/meti alos palsar. Alaska Satellite Facility, (ALP- SRP264684320).

Pardo, M., Vera, E., Yáñez, G., & Monfret, T. (2009). Tomografía sísmica bajo los Andes de Chile Central (33–34.5 S): Implicaciones sismotectónicas, Congreso Geológico Chileno, pp. S9–S067.

Pavez, C., Tapia, F., Comte, D., Gutierrez, F., Lira, E., Charrier, R., & Benavente, O. (2016). Characterization of the hydrothermal system of the Tinguiririca Volcanic Complex, Central Chile, using structural geology and passive seismic tomography. *Journal of Volcanology and Geothermal Research*, *310*, 107–117.

Peacock, J., Kirkby, A.L., Zhang, F., Hassan, R., & Duan, J. (2019). MTPy: A Python toolbox for magnetotelluric data. AGUFM 2019, NS21A-06.

Perez-Flores, P., Cembrano, J., Sanchez-Alfaro, P., Veloso, E., Arancibia, G., & Roquer, T. (2016). Tectonics, magmatism and paleo-fluid distribution in a strike-slip setting: Insights from the northern termination of the Liquine-Ofqui fault System, Chile. *Tectonophysics*, *680*, 192–210.

Perez-Flores, P., Veloso, E., Cembrano, J., Sanchez-Alfaro, P., Lizama, M., & Arancibia, G. (2017). Fracture network, fluid pathways and paleostress at the Tolhuaca geothermal field. *Journal of Structural Geology*, *96*, 134–148.

Piquer, J., Berry, R. F., Scott, R. J., & Cooke, D. R. (2016). Arc-oblique fault systems: Their role in the Cenozoic structural evolution and metallogenesis of the Andes of central Chile. *Journal of Structural Geology*, *89*, 101–117.

Piquer, J., Hollings, P., Rivera, O., Cooke, D. R., Baker, M., & Testa, F. (2017). Along-strike segmentation of the Abanico Basin, central Chile: New chronological, geochemical and structural constraints. *Lithos*, *268*, 174–197.

Piquer, J., Skarmeta, J., & Cooke, D. R. (2015). Structural evolution of the Rio Blanco-Los Bronces District, Andes of Central Chile: Controls on stratigraphy, magmatism, and mineralization. *Economic Geology*, *110*, 1995–2023.

Piquer, J., Yanez, G., Rivera, O., & Cooke, D. R. (2019). Long-lived crustal damage zones associated with fault intersections in the high Andes of Central Chile. *Andean Geology*, *46*, 223–239.

Pommier, A. (2014). Interpretation of magnetotelluric results using laboratory measurements. *Surveys in Geophysics*, *35*, 41–84.

Pritchard, M. E., Jay, J. A., Aron, F., Henderson, S. T., & Lara, L. E. (2013). Subsidence at southern Andes volcanoes induced by the 2010 Maule, Chile earthquake. *Nature Geoscience*, *6*, 632–636.

Ramos, V. A. (2010). The tectonic regime along the Andes: Present-day and Mesozoic regimes. *Geological Journal*, *45*, 2–25.

Ramos, V. A., Litvak, V. D., Folguera, A., & Spagnuolo, M. (2014). An Andean tectonic cycle: From crustal thickening to extension in a thin crust (34°–37° SL). *Geoscience Frontiers*, *5*, 351–367.

Richards, J. P., Boyce, A. J., & Pringle, M. S. (2001). Geologic evolution of the Escondida area, northern Chile: A model for spatial and temporal localization of porphyry cu mineralization. *Economic Geology and the Bulletin of the Society of Economic Geologists*, *96*, 271–305.

Roquer, T., Arancibia, G., Rowland, J., Iturrieta, P., Morata, D., & Cembrano, J. (2017). Fault-controlled development of shallow hydrothermal systems: Structural and mineralogical insights from the Southern Andes. *Geothermics*, *66*, 156–173.

Rowland, J. V., & Sibson, R. H. (2004). Structural controls on hydrothermal flow in a segmented rift system, Taupo Volcanic Zone, New Zealand. *Geofluids*, *4*, 259–283.

Rowland, J. V., & Simmons, S. F. (2012). Hydrologic, magmatic, and tectonic controls on hydrothermal flow, Taupo Volcanic Zone, New Zealand: Implications for the formation of epithermal vein deposits. *Economic Geology*, *107*, 427–457.

Sanchez, P., Perez-Flores, P., Arancibia, G., Cembrano, J., & Reich, M. (2013). Crustal deformation effects on the chemical evolution of geothermal systems: The intra-arc Liquine-Ofqui fault system, Southern Andes. *International Geology Review*, *55*, 1384–1400.

Sanchez-Alfaro, P., Sielfeld, G., Van Campen, B., Dobson, P., Fuentes, V., Reed, A., et al. (2015). Geothermal barriers, policies and economics in Chile—Lessons for the Andes. *Renewable and Sustainable Energy Reviews*, *51*, 1390–1401.

Sernageomin, S. (2003). Mapa Geológico de Chile: Versión digital. Servicio Nacional de Geología y Minería, Publicación Geológica Digital, No. 4 CD-Room, versión 1.0, base geológica escala 1.

Shaw, H. R. (1980). The fracture mechanisms of magma transport from the mantle to the surface. *Physics of Magmatic Processes*, *64*, 201–264.

Sibson, R. H. (1985). A note on fault reactivation. *Journal of Structural Geology*, *7*, 751–754.

Sibson, R. H. (1996). Structural permeability of fluid-driven fault-fracture meshes. *Journal of Structural Geology*, *18*, 1031–1042.

Sibson, R. H. (2004). Controls on maximum fluid overpressure defining conditions for mesozonal mineralisation. *Journal of Structural Geology*, *26*, 1127–1136.

Sielfeld, G., Cembrano, J., & Lara, L. (2017). Transtension driving volcano-edifice anatomy: Insights from Andean transverse-to-the-orogen tectonic domains. *Quaternary International*, *438*, 33–49.

Sielfeld, G., Lange, D., & Cembrano, J. (2019). Intra-arc crustal seismicity: Seismotectonic implications for the Southern Andes Volcanic Zone, Chile. *Tectonics*, *38*, 552–578. https://doi.org/10.1029/2018TC004985

Sillitoe, R. (1997). Characteristics and controls of the largest porphyry copper-gold and epithermal gold deposits in the circum-Pacific region. *Australian Journal of Earth Sciences*, *44*, 373–388.

Simpson, F., & Bahr, K. (2005). *Practical magnetotellurics*. Cambridge, UK: Cambridge University Press.

Smith, J. D., White, R. S., Avouac, J. P., & Bourne, S. (2020). Probabilistic earthquake locations of induced seismicity in the Groningen region, the Netherlands. *Geophysical Journal International*, *222*, 507–516.

Stanton-Yonge, A., Griffith, W. A., Cembrano, J., St Julien, R., & Iturrieta, P. (2016). Tectonic role of margin-parallel and margin-transverse faults during oblique subduction in the Southern Volcanic Zone of the Andes: Insights from boundary element modeling. *Tectonics*, *35*, 1990–2013. https://doi.org/10.1002/2016TC004226

Stern, C. R. (2007). Chilean volcanoes. In *The Geology of Chile* (pp. 147–178). London, UK: Geological Society of London.

Suzuki, Y., Ioka, S., & Muraoka, H. (2014). Determining the maximum depth of hydrothermal circulation using geothermal mapping and seismicity to delineate the depth to brittle-plastic transition in Northern Honshu, Japan. *Energies*, *7*, 3503–3511.

Tardani, D., Reich, M., Roulleau, E., Takahata, N., Sano, Y., Perez-Flores, P., et al. (2016). Exploring the structural controls on helium, nitrogen and carbon isotope signatures in hydrothermal fluids along an intra-arc fault system. *Geochimica et Cosmochimica Acta*, *184*, 193–211.

Tassi, F., Aguilera, F., Benavente, O., Paonita, A., Chiodini, G., Caliro, S., et al. (2016). Geochemistry of fluid discharges from Peteroa volcano (Argentina-Chile) in 2010–2015: Insights into compositional changes related to the fluid source region (s). *Chemical Geology*, *432*, 41–53.

Teyssier, C., Tikoff, B., & Markley, M. (1995). Oblique plate motion and continental tectonics. *Geology*, *23*, 447–450.

Tibaldi, A. (2005). Volcanism in compressional tectonic settings: Is it possible? *Geophysical Research Letters*, *32*, L06309. https://doi.org/10.1029/2004GL021798

Tikoff, B., & Teyssier, C. (1994). Strain modeling of displacement-field partitioning in transpressional orogens. *Journal of Structural Geology*, *16*, 1575–1588.

Turienzo, M., Dimieri, L., Frisicale, C., Araujo, V., & Sanchez, N. (2012). Cenozoic structural evolution of the Argentinean Andes at 34°40′ S: A close relationship between thick and thin-skinned deformation. Andean. *Geology*, *39*, 317–357.

Veloso, E. E., Tardani, D., Elizalde, D., Godoy, B. E., Sanchez-Alfaro, P. A., Aron, F., et al. (2019). A review of the geodynamic constraints on the development and evolution of geothermal systems in the Central Andean Volcanic Zone (18–28° Lat.S). *International Geology Review*, *62*(10), 1294–1318.

Viramonte, J., Galliski, M., Saavedra, V.A., Aparicio, A., García-Cacho, G., & Escorza, C. M. (1984). El finivulcanismo básico de la depresión de Arizaro, provincia de Salta. IX Cong. Geol. A rg., Actas 3, 234–251.

Waldhauser, F., & Ellsworth, W. L. (2000). A double-difference earthquake location algorithm: Method and application to the northern Hayward fault, California. *Bulletin of the Seismological Society of America*, *90*, 1353–1368.

Wannamaker, P. E., Caldwell, T. G., Jiracek, G. R., Maris, V., Hill, G. J., Ogawa, Y., et al. (2009). Fluid and deformation regime of an advancing subduction system at Marlborough, New Zealand. *Nature*, *460*(7256), 733–736. https://doi.org/10.1038/nature08204

Wrage, J., Tardani, D., Reich, M., Daniele, L., Arancibia, G., Cembrano, J., et al. (2017). Geochemistry of thermal waters in the Southern Volcanic Zone, Chile—Implications for structural controls on geothermal fluid composition. *Chemical Geology*, *466*, 545–561.

Yáñez, G. A., Gana, P., & Fernández, R. (1998). Origen y significado geológico de la Anomalía Melipilla, Chile central. *Revista Geologica de Chile*, *25*, 175–198.